

RESEARCH ARTICLE

10.1002/2016JC011821

The plumbing of the global biological pump: Efficiency control through leaks, pathways, and time scales

Benoît Pasquier¹ and Mark Holzer^{1,2}¹Department of Applied Mathematics, School of Mathematics and Statistics, University of New South Wales, New South Wales, Sydney, Australia, ²Also at Department of Applied Physics and Applied Mathematics, Columbia University, New York City, New York, USA

Key Points:

- Phosphorus pathways are systematically diagnosed for their contributions to the biological pump and their sequestration rates and times
- The Southern Ocean euphotic zone is where $(62 \pm 2)\%$ of regenerated PO_4 reemerges after a mean sequestration time of 240 ± 60 years
- Intermediate waters carry $\sim 1/3$ of the regenerated PO_4 exported from the equatorial Pacific that is destined for the Southern Ocean

Correspondence to:

B. Pasquier,
b.pasquier@student.unsw.edu.au

Citation:

Pasquier, B., and M. Holzer (2016), The plumbing of the global biological pump: Efficiency control through leaks, pathways, and time scales, *J. Geophys. Res. Oceans*, 121, 6367–6388, doi:10.1002/2016JC011821.

Received 22 MAR 2016

Accepted 1 AUG 2016

Accepted article online 6 AUG 2016

Published online 27 AUG 2016

Abstract We systematically quantify the pathways and time scales that set the efficiency, E_{bio} , of the global biological pump by applying Green-function-based diagnostics to a data-assimilated phosphorus cycle embedded in a jointly assimilated ocean circulation. We consider “bio pipes” that consist of phosphorus paths that connect specified regions of last biological utilization with regions where regenerated phosphate first reemerges into the euphotic zone. The bio pipes that contribute most to E_{bio} connect the Eastern Equatorial Pacific (EEqP) and Equatorial Atlantic to the Southern Ocean ($(21 \pm 3)\%$ of E_{bio}), as well as the Southern Ocean to itself ($(15 \pm 3)\%$ of E_{bio}). The bio pipes with the largest phosphorus flow rates connect the EEqP to itself and the subantarctic Southern Ocean to itself. The global mean sequestration time of the biological pump is 130 ± 70 years, while the sequestration time of the bio pipe from anywhere to the Antarctic region of the Southern Ocean is 430 ± 30 years. The distribution of phosphorus flowing within a given bio pipe is quantified by its transit-time partitioned path density. For the largest bio pipes, $\sim 1/7$ of their phosphorus is carried by thermocline paths with transit times less than ~ 300 – 400 years, while $\sim 4/7$ of their phosphorus is carried by abyssal paths with transit times exceeding ~ 700 years. The path density reveals that Antarctic Intermediate Water carries about a third of the regenerated phosphate last utilized in the EEqP that is destined for the Southern Ocean euphotic zone. The Southern Ocean is where $(62 \pm 2)\%$ of the regenerated inventory and $(69 \pm 1)\%$ of the preformed inventory first reemerge into the euphotic zone.

1. Introduction

The biological pump removes organic matter from the surface ocean and sequesters carbon at depth [e.g., Raven and Falkowski, 1999; Archer *et al.*, 2000] and therefore plays a crucial role in the atmosphere-ocean carbon balance, with implications for climate change and ocean acidification [e.g., Broecker, 1982; Marinov *et al.*, 2008a, 2008b; Sigman *et al.*, 2010]. The efficiency of the biological pump is set by the interplay of the ocean's advective-diffusive circulation with the biological uptake of nutrients and subsequent biogenic particle transport and remineralization. This interplay between the physical and biogenic transport of nutrients shapes the global ocean ecosystem and establishes the global-scale teleconnections between nutrient utilization in one region and nutrient resupply, and ultimately biological production, in another region. The paths and flow rates that mediate these teleconnections constitute the “plumbing” of the biological pump. Here we systematically diagnose the nutrient pathways throughout the world oceans to quantify how this “plumbing” controls the global efficiency of the biological pump.

Because phosphate (PO_4) is necessary in the metabolism of all phytoplankton, it is common to approximate PO_4 as the limiting nutrient and key all biological production to the phosphorus cycle [e.g., Smith, 1984; Howarth, 1988], an approach we will follow here. Early studies quantified the efficiency of the biological pump in terms of the vertical gradients of dissolved organic carbon [e.g., Volk and Hoffert, 1985]. More recently, the biological pump efficiency has been defined in terms of regenerated phosphate by Ito and Follows [2005] to explore the sensitivity of the atmospheric CO_2 partial pressure to oceanic nutrient draw-down. Here we extend their study to analyze the circulation control on biological pump efficiency in detail. Over the last decade, a number of studies have addressed the high-latitude control on global nutrient cycles [e.g., Sarmiento *et al.*, 2004; Marinov *et al.*, 2006]. Primeau *et al.* [2013] used a simple data-assimilated phosphorus cycling model to investigate the response of the pump efficiency to altered nutrient utilization in the Southern Ocean. Holzer and Primeau [2013] investigated the pathways and time scales that connect

utilization in the Southern Ocean with production in the subtropical and subpolar gyres of the North Atlantic, and how these change when Southern Ocean utilization is perturbed. A complementary study by *Palter et al.* [2010] used synthetic tracers within an ocean model to quantify the importance of various water masses, as well as the role of the overturning circulation in returning nutrients to the pycnocline. We extend and generalize these studies by systematically analyzing the global distribution of the pathways and time scales of the combined physical/biogenic nutrient transport in the current state of the ocean and how these control the global efficiency of the biological pump. Our work is a natural extension and generalization of the study by *DeVries et al.* [2012] who related the distribution of times with which exported phosphate remains in the aphotic interior to the efficiency of the biological pump in terms of a geographically distributed sequestration efficiency.

Here we systematically analyze the ocean's nutrient cycling to address the following key questions:

1. What is the geographic distribution of the biological pump and its leaks?
2. What are the dominant connections between nutrient uptake and nutrient resupply across the world oceans?
3. What are the three-dimensional pathways, time scales, and flow rates that mediate these connections and how much do they contribute to the efficiency of the biological pump?

Our analysis quantifies the contributions of the global preformed and regenerated nutrient pathways to the biological pump efficiency. Pathways are quantified not only in terms of the geographic connections between nutrient suppliers and receptors, but also in terms of the three-dimensional, transit-time partitioned nutrient path density. The dominant contributors to the biological pump efficiency are paths from productive equatorial regions to the Southern Ocean (SO) as well as SO-to-SO "trapped" paths. The SO is thus not only the biological pump's primary leak providing most of the world ocean's preformed nutrients, but also the preferred destination of regenerated nutrients. A key pathway of regenerated nutrients to the SO is via recirculating Antarctic Intermediate Water (AAIW) accessed in tropical and subtropical regions through biogenic particle transport.

2. Model

2.1. Circulation

We use the data-assimilated, steady nonseasonal circulation of *Primeau et al.* [2013], which is similar to that of *DeVries and Primeau* [2011] except that the horizontal resolution has been increased to $2^\circ \times 2^\circ$, and CFC-11 and PO_4 have been incorporated as tracer constraints in addition to temperature, salinity, and radiocarbon. The circulation is constrained dynamically and the data assimilation used the wind-stress climatology of *Trenberth et al.* [1989] and specified horizontal and vertical viscosities of $A_h = 5 \times 10^4 \text{ m}^2 \text{ s}^{-1}$ and $A_v = 10^{-4} \text{ m}^2 \text{ s}^{-1}$. The circulation's advective-diffusive transport operator has fixed horizontal and vertical eddy diffusivities of 10^3 and $10^{-5} \text{ m}^2 \text{ s}^{-1}$, respectively. While the diffusivity tensor is not aligned with the isopycnals, the data assimilation adjusts the velocity field such that the overall advection-diffusion results in tracer fields and heat and freshwater transports that have high fidelity to the observations [*DeVries and Primeau*, 2011]. Although it is possible that the velocity field has some unrealistic features to compensate for the nonrotated diffusivity, the integrated transport of tracers is well captured. (This is underscored by the fact that if we repeat our calculations with the newer data-assimilated circulations of *DeVries* [2014] that all have a rotated diffusivity, we obtain virtually identical results, albeit with a slightly worse fit to the PO_4 field, which was not assimilated by *DeVries* [2014].) We emphasize that the circulation used effectively provides a ventilation-weighted transport because it has been optimized against PO_4 and the ventilation tracers CFC-11 and radiocarbon. The steady model circulation, which has no seasonal cycle, thus does not bias estimates of preformed nutrients as an annual-average circulation would.

2.2. Phosphorus Cycle

We base our diagnostics on a simple steady model of the phosphorus cycle that was jointly assimilated with the physical circulation by *Primeau et al.* [2013]. The optimized control variables of the phosphorus cycle are the phosphate uptake field, the Martin exponent of the organic particle-flux profile (approximated as globally uniform), and the global phosphate inventory. The assimilation included a nonsmoothness penalty for the uptake field. For details see the work of *Primeau et al.* [2013], where the model's export

production, regenerated and preformed phosphate fields, and dissolved organic phosphorus (DOP) distributions are documented. The root-mean-square (RMS) volume-weighted mismatch between modeled and observed $[PO_4]$ is a mere 4% of the global mean with no systematic biases. Because the phosphorus cycle was jointly assimilated with the circulation, the steady ventilation-weighted circulation does not inappropriately bias the phosphorus cycle toward winter conditions. The model's global preformed PO_4 inventory is $(61 \pm 4)\%$, which compares well with an independent estimate of 59% based on apparent oxygen utilization [Primeau et al., 2013].

The phosphorus cycle explicitly transports inorganic phosphate (PO_4) and dissolved organic phosphorus (DOP) and couples them via remineralization and biological utilization. Denoting the concentrations of PO_4 and DOP by P_I and P_O , respectively, we write the phosphorus tracer equations as

$$\frac{\partial}{\partial t} \begin{bmatrix} P_I \\ P_O \end{bmatrix} + \begin{bmatrix} \mathcal{T} + \gamma & -\kappa \\ 0 & \mathcal{T} + \kappa \end{bmatrix} \begin{bmatrix} P_I \\ P_O \end{bmatrix} = \begin{bmatrix} -\gamma_g(P_I - \bar{P}_I) \\ S\gamma P_I \end{bmatrix}, \quad (1)$$

where the operator \mathcal{T} is the advection-eddy-diffusion operator, $\gamma(\mathbf{r})$ is the PO_4 uptake rate constant at point \mathbf{r} , and κ is the globally uniform rate constant for remineralizing DOP. The uptake rate constants are diagnosed from the data-assimilated PO_4 uptake rate per unit volume, $J(\mathbf{r})$, as $\gamma(\mathbf{r}) = J(\mathbf{r})/P_I(\mathbf{r})$, which is nonzero only in the euphotic zone modeled as the upper 73.4 m of the water column (top two model layers). Note that equation (1) has precisely the same solution as the data-assimilated phosphorus cycle, but is completely linear in the PO_4 and DOP concentrations, allowing us to use Green-function-based diagnostics to trace phosphorus through the ocean [Primeau et al., 2013; Holzer and Primeau, 2013].

The source of DOP per unit volume is given by SJ , where the operator S instantaneously reassigns the PO_4 uptake per unit volume, $\gamma(\mathbf{r})P_I(\mathbf{r})$, to a source of DOP throughout the water column: a fraction σ of the uptake is reassigned to a source of DOP in the euphotic zone, while the remaining fraction $(1 - \sigma)$ becomes a DOP source proportional to the divergence of a power-law particle-flux profile in the aphotic zone (Martin exponent b)—see the work of Kwon and Primeau [2006] and Primeau et al. [2013] for details. In (1), the weak relaxation to the observed global mean phosphate concentration \bar{P}_I , with a “geological” (subscript g) restoring time scale $\gamma_g^{-1} = 10^6$ years, is introduced so that the total amount of phosphorus in the ocean is determined even for the steady-state equations (i.e., even without a specified initial phosphate field).

We use the parameter values $b = 0.70$, $\sigma = 1/3$, and $\kappa = (0.5 \text{ year})^{-1}$ of the data-assimilated phosphorus cycle. Only b was optimized, σ and κ were specified. The relative sensitivity of the preformed and regenerated phosphate fields to variations in these parameters is documented in the work of Primeau et al. [2013]. (The maximum zonally averaged relative sensitivities $(\kappa/P_{\text{reg}})\partial P_{\text{reg}}/\partial \kappa$ and $(\kappa/P_{\text{pre}})\partial P_{\text{pre}}/\partial \kappa$ lie in the upper ocean and are $\sim 20\%$.) In the analyses below, the uncertainty δX in a quantity X was estimated from the linear sensitivities to b , σ , and κ as $\delta X = \sqrt{(\partial_b X \delta b)^2 + (\partial_\sigma X \delta \sigma)^2 + (\partial_\kappa X \delta \kappa)^2}$. We took $\delta b = 0.35$, $\delta \sigma = 0.15$, and $\delta \kappa = (0.25 \text{ year})^{-1}$ as reasonable uncertainties in the parameters themselves.

3. Green-Function Diagnostics

The linearity of equation (1) enables the use of Green functions to trace phosphorus through its biogenic and physical transport paths [e.g., Primeau et al., 2013; Holzer and Primeau, 2013]. The fundamental Green function of the equation is obtained by replacing the source term on the right-hand side of (1) with $\delta(\mathbf{r} - \mathbf{r}') \delta(t - t') \mathbf{I}$, where \mathbf{I} is the 2×2 identity matrix, and by replacing $[P_I, P_O]^T$ with the corresponding response, that is, with the Green function

$$\mathbf{G} \equiv \begin{bmatrix} G_{II} & G_{IO} \\ G_{OI} & G_{OO} \end{bmatrix}, \quad (2)$$

which obeys the causality condition $\mathbf{G} = 0$ for $t < t'$. Matrix element $G_{II}(\mathbf{r}, t | \mathbf{r}', t')$ is the inorganic phosphate response at (\mathbf{r}, t) to an inorganic source at (\mathbf{r}', t') , G_{IO} is the inorganic remineralized phosphate response to a DOP source, G_{OO} is the DOP response to a DOP source, and $G_{OI} = 0$ because phosphate is not converted to DOP except through uptake, which we represented by a source in (1).

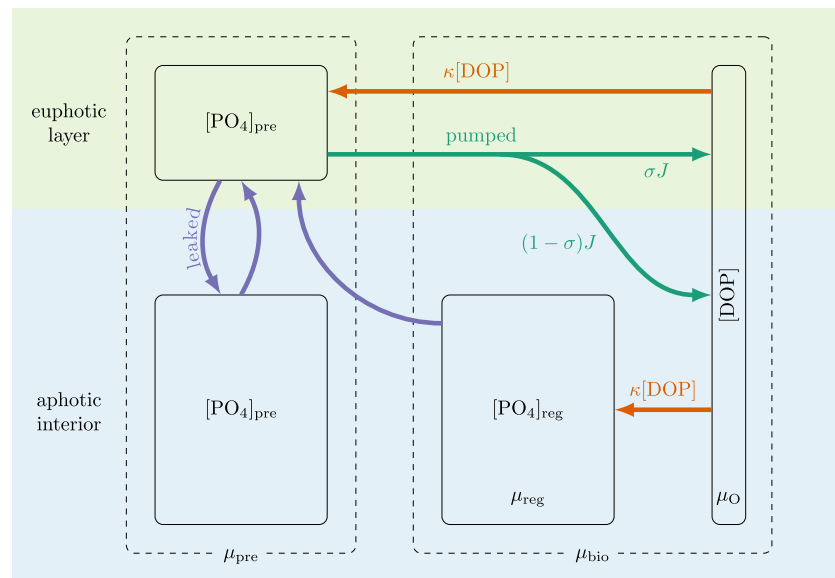


Figure 1. Schematic of the exchange between the phosphorus pools: euphotic and aphotic preformed phosphate (global mass μ_{pre}), regenerated phosphate (global mass μ_{reg}), and dissolved organic phosphorus (DOP, global mass μ_O). Blue arrows represent physical transport by the circulation. Both phosphate and DOP are transported as tracers in our model. Green arrows represent the biogenic particle transport of organic phosphorus and its dissolution into the DOP pool, which is instantaneous in our model. The DOP production rate is σJ in the euphotic zone and $(1-\sigma)J$ in the aphotic zone, with PO_4 uptake rate J . Orange arrows represent the remineralization of DOP with rate constant κ . The total mass of bio phosphorus is denoted by $\mu_{bio} = \mu_{reg} + \mu_O$.

From \mathbf{G} , we calculate regenerated and preformed phosphate as well as DOP at point (\mathbf{r}, t) partitioned according to the time t_i and region Ω_i where the phosphorus was last in the euphotic zone (preformed PO_4 , denoted by P_{pre}) or last utilized (regenerated PO_4 and DOP). Regenerated phosphate, denoted by P_{reg} , is remineralized DOP that has not yet been in contact with the euphotic layer. Once P_{reg} reemerges in the euphotic layer, it is relabeled as P_{pre} . The pathways and conversions between the phosphorus pools are illustrated schematically in Figure 1.

To partition phosphorus into P_{reg} and P_{pre} , and to compute the flux of first reemergence into the euphotic zone, we impose fast relaxation to zero in the euphotic zone with a time scale $\gamma_0^{-1} = 1$ s. The fast relaxation effectively imposes the boundary condition of zero regenerated phosphate in the euphotic zone – see also Appendices A and B. From here on, we additionally impose this fast relaxation on G_{IO} and G_{II} so that the inorganic component of \mathbf{G} is the Green function for the regenerated phosphate system.

Using a suitable adjoint of (1), we also partition phosphorus according to the time t_f and regions Ω_f where the phosphorus next emerges into the euphotic zone. From these partitioned quantities and their fluxes in and out of the euphotic zone, we can compute the mass, flow rate, and path-density distribution of phosphorus in transit from euphotic region Ω_i to euphotic region Ω_f (subscript index notation i and f for “initial” and “final”) as detailed in Appendices A and B.

4. Biological Pump Efficiency

Following Ito and Follows [2005], we define the global efficiency of the biological pump in terms of the preformed phosphate inventory. Denoting the global ocean inventory of phosphorus (in either mass units or moles) by μ_p and the inventory of phosphorus within preformed and regenerated phosphate by μ_{pre} and μ_{reg} , the global pump efficiency E_{bio} is defined by

$$E_{bio} \equiv \frac{\mu_p - \mu_{pre}}{\mu_p} = \frac{\mu_{reg} + \mu_O}{\mu_p} = \frac{\mu_{bio}}{\mu_p}. \quad (3)$$

In (3), we added the inventory of phosphorus in the form of DOP, μ_O , to account for all nonpreformed, biologically utilized phosphorus, or “bio phosphorus” for short. The inventory of bio phosphorus is $\mu_{bio} = \mu_{reg} + \mu_O$. While adding μ_O to μ_{reg} is necessary to account rigorously for all bio phosphorus, we

estimate μ_O to be a mere $(0.1 \pm 0.3)\%$ of μ_P in the current state of the ocean, and one could neglect μ_O and simply compute the efficiency as μ_{reg}/μ_P [e.g., Ito and Follows, 2005; Primeau et al., 2013]. Here we keep μ_O for completeness and to demonstrate that one can easily track biologically utilized phosphorus through the DOP pool before it becomes regenerated phosphate. The global biological pump efficiency for our estimate of the phosphorus cycle is $E_{bio} = (39 \pm 4)\%$ [Primeau et al., 2013].

5. Plumbing of the Biological Pump

We now investigate how the efficiency of the biological pump is set by the combined physical and biogenic transport of phosphorus between different geographic regions of the euphotic zone. To keep the analysis manageable, we subdivide the global euphotic zone into the 14 regions Ω_i defined in Figure 2. We identify individual regions with abbreviations of their geographic description (e.g., SAAD for South of Antarctic Divergence, NAAD for North of Antarctic Divergence, EEQP for Eastern Equatorial Pacific), all of which are given in the caption of Figure 2. These regions have been defined so that their boundaries are either contours of constant production, constant latitude, or, for the partition between the SAAD and NAAD regions, the locus of maximum Ekman divergence in the Southern Ocean.

5.1. Pumped and Leaked Phosphorus

Each region Ω_i contributes to the global pump efficiency through the amount of phosphorus that it provides to the pump, $\mu_{bio}(\Omega_i)$, or equivalently through the amount that escapes or “leaks” from the pump, $\mu_{pre}(\Omega_i)$. We therefore define the fractional bio-pump contributions $\beta(\Omega_i)$ and the fractional leak contributions $\lambda(\Omega_i)$ as

$$\beta(\Omega_i) \equiv \frac{\mu_{bio}(\Omega_i)}{\mu_P} \quad \text{and} \quad \lambda(\Omega_i) \equiv \frac{\mu_{pre}(\Omega_i)}{\mu_P}, \quad (4)$$

so that the global pump efficiency is simply determined by the total fraction pumped, $\sum_i \beta(\Omega_i)$, or equivalently by the total fraction leaked, $\sum_i \lambda(\Omega_i)$:

$$E_{bio} = \sum_i \beta(\Omega_i) = 1 - \sum_i \lambda(\Omega_i). \quad (5)$$

The inventories $\mu_{bio}(\Omega_i)$ and $\mu_{pre}(\Omega_i)$ from each region are computed as described in Appendices A and B.

Figure 3 shows the complementary views afforded by equation (5) of how different regions contribute to the global pump efficiency. The pumped fractions shown in the left slice of the pie partition the total pump efficiency of $(39 \pm 4)\%$. Highly productive regions contribute the most: the North of the Antarctic Divergence (NAAD), Equatorial Indian Ocean (EqInd), Eastern Equatorial Pacific (EEQP), Subpolar North Pacific (SubPoNP), and Equatorial Atlantic (EqA) regions account for $(74 \pm 8)\%$ of E_{bio} , with the EEQP making the largest contribution of $(25 \pm 4)\%$.

The corresponding leaked fractions are shown in the right slice of the pie of Figure 3, which partitions the $(61 \pm 4)\%$ global fraction of preformed phosphate that escaped biological utilization. The euphotic zones of the high-latitude oceans are the largest leak: the Southern Ocean (SAAD and NAAD) and the subpolar North Pacific and Atlantic regions (SubPoNP and SubPoNA) account for $(96 \pm 1)\%$ of the global leak, with the SAAD and NAAD regions contributing $(43 \pm 4)\%$ and $(32 \pm 1)\%$, respectively. The incomplete utilization of the abundantly available macronutrients in the Southern Ocean is due to a number of limiting factors, including low micronutrients [e.g., Dutkiewicz et al., 2006]. Equatorial regions have almost no leaks, with large-scale upwelling of nutrients being balanced by nearly complete nutrient utilization.

The relative size of the phosphorus amount pumped or leaked from a given region Ω_i can be summarized by defining a local biological pump efficiency for each Ω_i as the ratio of the bio phosphorus to the total phosphorus originating from Ω_i . These local efficiencies are indicated in Figure 2 on the map defining the Ω_i patches. Equatorial patches, which provide near-zero preformed phosphate because of the overall upwelling, stand out as being nearly 100% efficient. By contrast, the Southern Ocean and subpolar North Atlantic are very inefficient because they are major leaks. Subtropical regions are sources of both preformed phosphate and bio phosphorus, and hence of intermediate efficiency. The subpolar North Pacific is a region

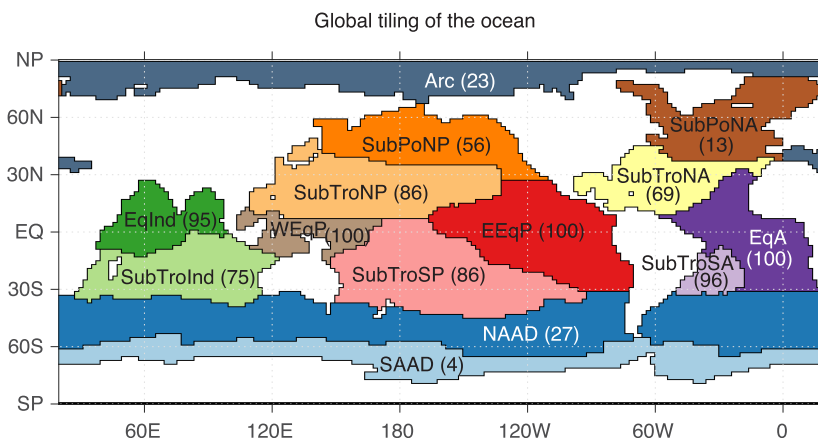


Figure 2. Partition of the global euphotic zone into 14 regions, denoted by Ω_i . The abbreviations that label the regions stand for: South of Antarctic Divergence (SAAD), North of Antarctic Divergence (NAAD), Subtropical South Atlantic (SubTroSA), Subtropical South Pacific (SubTroSP), Subtropical Indian Ocean (SubTroInd), Equatorial Atlantic (EqA), Eastern Equatorial Pacific (EEqP), Western Equatorial Pacific (WEqP), Equatorial Indian Ocean (EqInd), Subtropical North Atlantic (SubTroNA), Subtropical North Pacific (SubTroNP), Subpolar North Atlantic (SubPoNA), Subpolar North Pacific (SubPoNP), and Arctic (Arc). Non-Arctic regions plotted in saturated colors correspond to high-productivity regions (NAAD, EqInd, EEqP, SubPoNP, EqA, and SubPoNA). The numbers in parentheses are the local pump efficiencies of each region in percent, defined as $\mu_{\text{bio}}(\Omega_i \rightarrow \Omega) / \mu_p(\Omega_i \rightarrow \Omega)$, where Ω denotes the global euphotic zone.

of high production but includes regions of high phosphate so that, in spite of large-scale upwelling, enough preformed phosphate leaks out for a relatively low (60 ± 10)% local efficiency.

5.2. $\Omega_i \rightarrow \Omega_f$ Phosphorus “Pipes”

We now ask how much of the phosphate newly emerging into the euphotic zone of region Ω_f was last injected by the biological pump of region Ω_i and how much transited to Ω_f after leaking from the pump of Ω_i as preformed phosphate. Conceptually, we may consider the $\Omega_i \rightarrow \Omega_f$ transport as defining two $\Omega_i \rightarrow \Omega_f$ advective-diffusive “pipes”: “preformed pipes” that transport preformed phosphate and “bio pipes” that transport bio phosphorus that either remineralizes en route to, or within, destination region Ω_f . We emphasize that “pipe” here is not meant to suggest bulk-advective transport in any way and should not be confused with the purely advective nutrient streams considered by, e.g., *Pelegri and Csanady [1991]*, *Pelegri et al. [1996]*, and *Williams et al. [2006, 2011]*. Instead, we use the term as a convenient metaphor for organizing our discussion of the $\Omega_i \rightarrow \Omega_f$ flow of phosphorus. For each of the $14 \times 14 = 196$ $\Omega_i \rightarrow \Omega_f$ pipes, we now quantify the amount of phosphorus that is carried, the flow rate with which this phosphorus reemerges as phosphate in Ω_f , and the associated transport time scale of each pipe. These metrics quantify the global “plumbing” of the biological pump.

Figure 4 displays the fractions of the global phosphorus inventory, μ_p , in the $\Omega_i \rightarrow \Omega_f$ bio pipes, organized into a matrix so that rows correspond to origin (Ω_i) and columns correspond to destination (Ω_f). Summing these fractions over all possible $\Omega_i \rightarrow \Omega_f$ bio pipes yields the global biological pump efficiency, E_{bio} . Figure 4 thus quantifies both the mass within the $\Omega_i \rightarrow \Omega_f$ bio pipe and its contribution to E_{bio} . The 11 bio pipes carrying the largest phosphorus mass ($(20 \pm 4)\%$ of μ_p) account for $(52 \pm 6)\%$ of E_{bio} . The pattern of the $\Omega_i \rightarrow \Omega_f$ connections shows that highly productive equatorial regions, the NAAD region of the Southern Ocean and the subpolar North Pacific supply regenerated phosphate to either themselves (the relatively large diagonal terms) or to regions of subpolar upwelling, especially the SAAD region of the Southern Ocean. The diagonal terms quantify physical nutrient trapping whereby organic phosphorus exported by biogenic particle transport is remineralized and returned to the euphotic zone through subsurface convergence and upwelling [e.g., *Primeau et al., 2013; Holzer et al., 2014*]. The subpolar regions are important conduits that connect to the interior nutrient pool through isopycnal transport along outcropping density surfaces and through convective vertical mixing: $(62 \pm 2)\%$ of the bio phosphorus inventory is destined for reexposure in the Southern Ocean.

Figure 4 also shows the fractions of μ_p in the $\Omega_i \rightarrow \Omega$ and $\Omega \rightarrow \Omega_f$ bio pipes, where Ω denotes the global euphotic zone ($\Omega = \sum_k \Omega_k$). Each $\Omega_i \rightarrow \Omega$ fraction is represented as a horizontal bar on the left of the

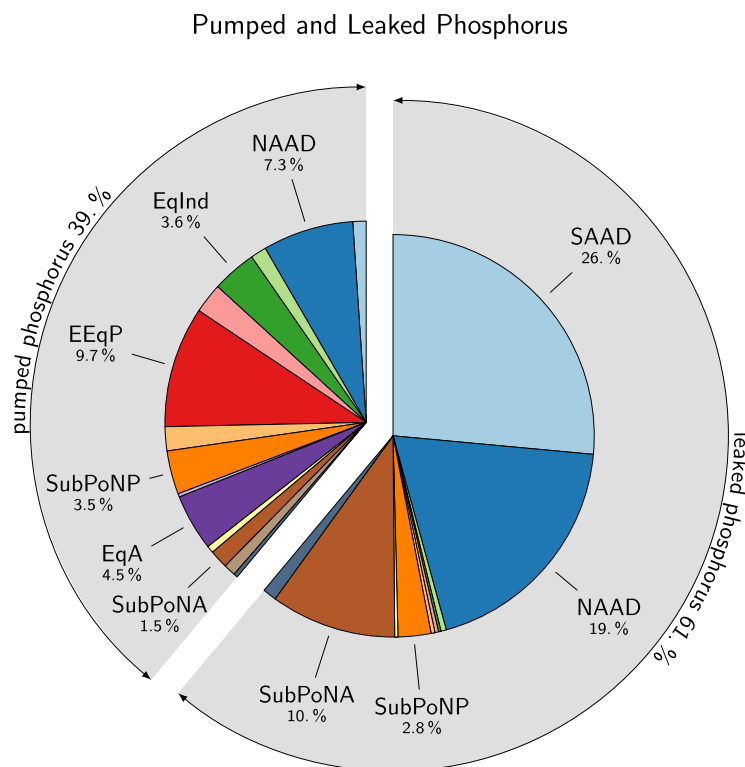


Figure 3. The biologically pumped and leaked fractions of phosphorus for each region Ω_i color-coded as in Figure 2. On the left, the fractions $\beta(\Omega_i) \equiv \mu_{\text{bio}}(\Omega_i)/\mu_p$ represent the contribution of each patch to the global biological pump efficiency. On the right, the fractions $\lambda(\Omega_i) \equiv \mu_{\text{pre}}(\Omega_i)/\mu_p$ represent the contribution of each patch to the global pump leak (global preformed phosphate inventory).

Southern Ocean trapped paths are the dominant contributors with $(53 \pm 2)\%$ of the global preformed PO_4 inventory ($(32 \pm 1)\%$ of μ_p) in $\text{SO} \rightarrow \text{SO}$ transit. The $\Omega_i \rightarrow \Omega$ fractions (left bar graph) are by definition equal to the leak contributions $\lambda(\Omega_i)$ of Figure 3. The $\Omega \rightarrow \Omega_f$ fractions (top bar graph) show that regardless of origin, $(69 \pm 1)\%$ of preformed phosphate ($(42 \pm 2)\%$ of μ_p) is in transit to the Southern Ocean euphotic zone. The Southern Ocean euphotic zone is thus not only the main leak of the biological pump, but also the primary recipient of preformed phosphate.

The patterns of $\mu_{\text{bio}}(\Omega \rightarrow \Omega_f)$ and $\mu_{\text{pre}}(\Omega \rightarrow \Omega_f)$ in Figures 4 and 5 are remarkably similar: Regenerated and preformed phosphate reemerge into the euphotic zone with a common geographic pattern. This is consistent with the fact that the bulk of preformed phosphate enters the ocean interior at deep-water formation sites and is hence primarily injected into deep waters, much like bio phosphorus that has access to deep waters through biogenic particle transport. Thus, preformed phosphate and bio phosphorus, while having different source distributions, reemerge with a similar pattern where deep waters upwell and/or are mixed back to the surface.

5.3. Flow Rates of Bio Phosphorus

The phosphorus masses in the bio pipes set the global efficiency of the biological pump, but by themselves they do not determine the $\Omega_i \rightarrow \Omega_f$ transport rates. We now examine the $\Omega_i \rightarrow \Omega_f$ flow rates and the corresponding mean transport time scales. We only consider bio pipes here because the flow rates of preformed phosphate are completely dominated by short paths connecting Ω_i to itself or an abutting region. The dominance of these short paths is due to an underlying diffusive singularity that has been documented in a number of contexts [e.g., Hall and Holzer, 2003; Primeau and Holzer, 2006]. For finite numerical resolution, this singularity is not realized, resulting in merely large but not infinite self-connections. For the bio pipes, however, these diffusive singularities would not even manifest in the continuum limit because the flow rates are limited by (i) finite uptake in Ω_i (finite pumping) and by (ii) finite remineralization rate as all

corresponding Ω_i row, and each $\Omega \rightarrow \Omega_f$ fraction is represented as a vertical bar on top of the corresponding Ω_f column. The $\Omega_i \rightarrow \Omega$ fractions are by definition equal to the pumped fractions $\beta(\Omega_i)$ of Figure 3. The $\Omega \rightarrow \Omega_f$ fractions show that the SO is where $(62 \pm 2)\%$ of the global bio phosphorus inventory ($(24 \pm 3)\%$ of μ_p) first reemerges into the euphotic zone as remineralized PO_4 . Outside the SO, $(13 \pm 1)\%$ and $(10 \pm 1)\%$ of the global bio phosphorus inventory first reemerge as PO_4 in the SubPoNP and EEqP euphotic zones.

Figure 5 displays the fractions of the global phosphorus inventory, μ_p , in the preformed $\Omega_i \rightarrow \Omega_f$ pipes: These fractions quantify the size of the purely circulation-driven $\Omega_i \rightarrow \Omega_f$ preformed pipes and their contribution to the global pump leak.

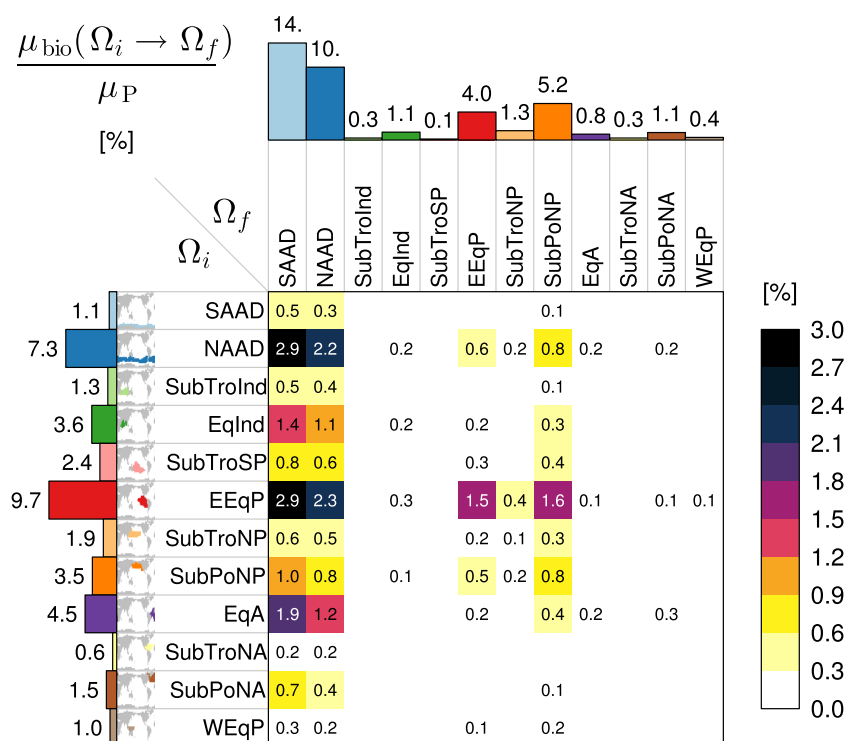


Figure 4. Percentage contributions to the biological pump efficiency E_{bio} by the $\Omega_i \rightarrow \Omega_f$ bio pipes that connect last phosphate uptake in Ω_i to first phosphate reexposure in Ω_f , organized into matrix form. The left and top bar graphs are sums over Ω_f and Ω_i , respectively. The left bars thus represent the Ω_i -to-anywhere contributions to E_{bio} , and the top bars represent the anywhere-to- Ω_f contributions to E_{bio} . Summed over all matrix elements, these percentages sum to the $E_{\text{bio}} = (39 \pm 4)\%$ efficiency of the biological pump. The global inventory of bio phosphorus is $\mu_{\text{bio}}(\Omega \rightarrow \Omega) = 1.1 \text{ Pmol}$. For clarity, contributions less than 0.1% have been omitted.

phosphorus in the bio pipes first passes through the DOP pool. The $\Omega_i \rightarrow \Omega_i$ self-connections are still expected to have the largest flow rates because eddy diffusion provides the fastest route back to Ω_i .

Figure 6 displays the flow rates $\Phi_{\text{bio}}(\Omega_i \rightarrow \Omega_f)$ of the bio pipes, normalized by the corresponding global flow rate, $\Phi_{\text{bio}}(\Omega \rightarrow \Omega)$, where Ω again denotes the global euphotic zone. The expected dominance of the eddy-diffusive transport for self-connections can be seen in the diagonal elements $\Omega_i = \Omega_f$, which are finite but at least an order of magnitude larger than all other terms. Because the flow rate in the $\Omega_i \rightarrow \Omega_f$ bio pipe is set by the uptake rate in Ω_i , the largest flow rates connect highly productive regions to themselves: NAAD ($16 \pm 3\%$), EEqP ($16 \pm 4\%$), EqA ($7 \pm 2\%$), SubPoNP ($6 \pm 1\%$), and EqInd ($5 \pm 1\%$), which together account for ($49 \pm 8\%$) of the total flow rate in all bio pipes. A change in κ^{-1} by ± 0.25 year results in less than 10% changes in the self-teleconnection flow rates. (See Appendix C for details on the sensitivity of DOP and the remineralization rate κP_O to changes in κ .)

Figure 6 also shows the $\Omega_i \rightarrow \Omega$ (left bar graphs) and $\Omega \rightarrow \Omega_f$ (top bar graphs) flow rates. The pattern of the $\Omega_i \rightarrow \Omega$ flow rates is very similar to the pattern of the amount of bio phosphorus in the corresponding $\Omega_i \rightarrow \Omega$ pipes (Figure 4), suggesting that $\Phi_{\text{bio}}(\Omega_i \rightarrow \Omega)$ and $\mu_{\text{bio}}(\Omega_i \rightarrow \Omega)$ are approximately proportional at least for these large regions. The flow rates regardless of origin ($\Omega \rightarrow \Omega_f$) are largest for the SO and EEqP receptors, both of which are characterized by strong nutrient trapping (self-connections) that is the dominant contribution to their $\Omega \rightarrow \Omega_f$ flow rates.

The bio pipes that make the largest contributions to E_{bio} are those that carry the largest bio phosphorus mass, which does not necessarily correspond to the strongest flow rate. For example, the NAAD \rightarrow SAAD and EEqP \rightarrow SAAD bio pipes together account for ($15 \pm 2\%$) of the total mass of bio phosphorus, μ_{bio} , but only for ($5 \pm 3\%$) of the total flow rate. Conversely, the NAAD \rightarrow NAAD and EEqP \rightarrow EEqP bio pipes together only account for ($10 \pm 1\%$) of the total μ_{bio} , but for ($32 \pm 5\%$) of the flow rate. The natural link between the mass and flow rate of the bio pipes is a measure of the mean time within the pipe, which we examine next.

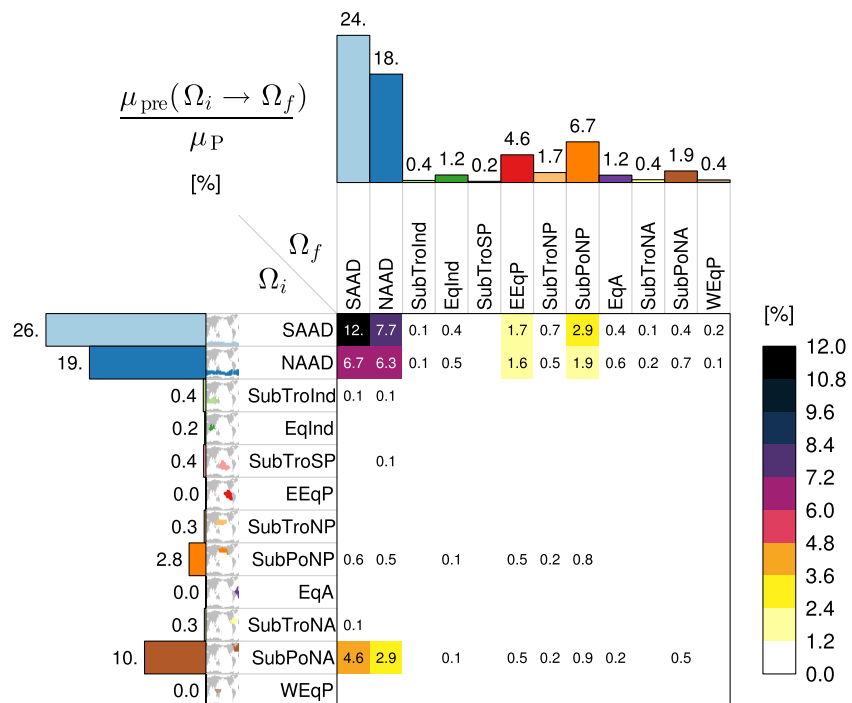


Figure 5. Percentage contributions to the biological pump leak by the $\Omega_i \rightarrow \Omega_f$ "preformed pipes" that connect last contact with the euphotic zone in Ω_i to first reexposure in Ω_f , organized into matrix form. The left and top bar graphs are sums over Ω_f and Ω_i , respectively. The left bars thus represent the Ω_i -to-anywhere contributions to the pump leak, and the top bars represent the anywhere-to- Ω_f contributions to the pump leak. Summed over all matrix elements, these percentages sum to the $(61 \pm 4)\%$ leak of the biological pump. The global inventory of preformed phosphorus is $\mu_{\text{pre}}(\Omega \rightarrow \Omega) = 1.7 \text{ Pmol}$. For clarity, contributions less than 0.1% have been omitted.

5.4. Time Scales

The time scale Γ_{bio} defined for the $\Omega_i \rightarrow \Omega_f$ pipe by the ratio

$$\Gamma_{\text{bio}}(\Omega_i \rightarrow \Omega_f) \equiv \frac{\mu_{\text{bio}}(\Omega_i \rightarrow \Omega_f)}{\Phi_{\text{bio}}(\Omega_i \rightarrow \Omega_f)}, \quad (6)$$

is the mean age on exit for phosphorus analogous to the mean age on exit for fluid defined by *Holzer et al.* [2012]. Γ_{bio} is the mean transit time from Ω_i to Ω_f averaged over the population of bio phosphorus molecules last utilized in Ω_i that reemerge into the euphotic zone of Ω_f either as regenerated PO_4 , or as DOP that remineralizes there. Equivalently, because we are in steady state, Γ_{bio} is also the mean $\Omega_i \rightarrow \Omega_f$ transit time averaged over the population of phosphorus molecules utilized in Ω_i that are destined for reemergence in Ω_f as regenerated PO_4 or as DOP that remineralizes in Ω_f . (Γ_{bio} is also the first temporal moment of the transit-time partitioned flow-rate distribution \mathcal{J}_{bio} —see Appendix A.) The phosphorus mean age on exit should not be confused with the mean transit time of phosphorus averaged over the population in transit in the ocean interior, which is typically much longer [*Holzer et al.*, 2012; *Holzer and Primeau*, 2013]. The time scale Γ_{bio} is also naturally interpreted as a mean sequestration time because, in steady state, it is the mean time that the population of bio phosphorus molecules entering the interior at Ω_i spends in the interior before reemerging into the euphotic zone at Ω_f .

Figure 7 shows the mean sequestration times Γ_{bio} for all $\Omega_i \rightarrow \Omega_f$, $\Omega_i \rightarrow \Omega_i$, and $\Omega \rightarrow \Omega_f$ bio pipes, as well as for the global $\Omega \rightarrow \Omega$ bio pipe. The longest mean sequestration times of 13–16 centuries are associated with phosphorus paths beginning in the North and tropical Atlantic and ending in the euphotic zone of the Indian and Pacific Oceans. The biogenic particle transport accesses North Atlantic Deep Water, which then carries the phosphorus to these destinations in the deep branch of the diffusive conveyor [*Holzer and Primeau*, 2006, 2008]. However, these paths make only minor contributions to the biological pump efficiency because the corresponding flow rates are small and translate to small masses of bio phosphorus. The bio pipes exiting in the Southern Ocean, all of which make significant contributions to E_{bio} , are characterized by mean ages on exit that range from ~ 50 years (for NAAD \rightarrow NAAD) to ~ 980 years (for SubPoNP \rightarrow SAAD).

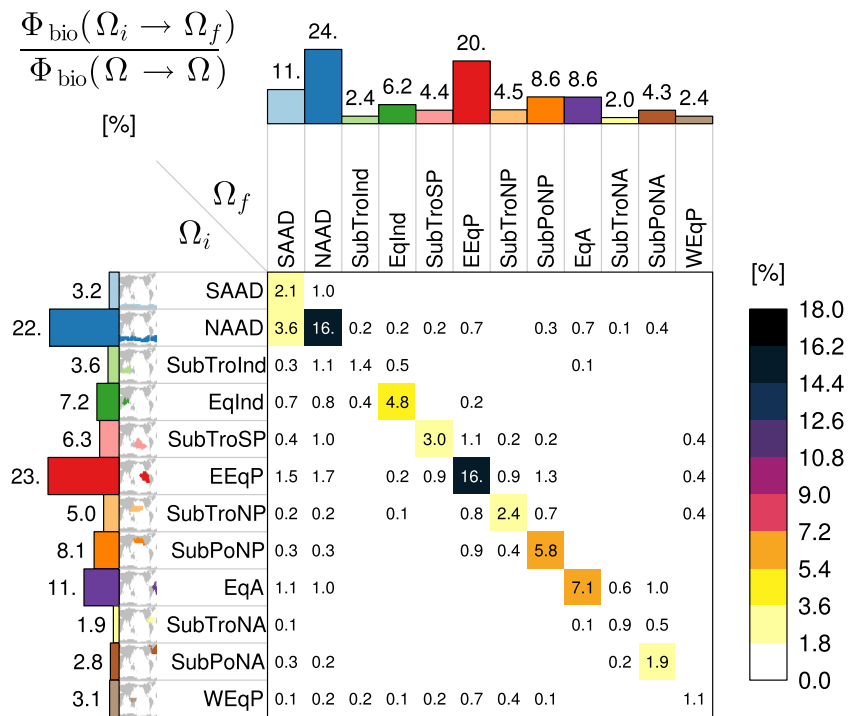


Figure 6. The normalized flow rates, Φ_{bio} , of the $\Omega_i \rightarrow \Omega_f$ bio pipes organized as in Figure 4. The flow rates have been normalized by the anywhere-to-anywhere ($\Omega \rightarrow \Omega$) flow rate of bio phosphorus and are expressed as a percentage. The left and top bar graphs are sums over Ω_f and Ω_i , representing the $\Omega_i \rightarrow \Omega$ and $\Omega \rightarrow \Omega_f$ flow rates, respectively. The global anywhere-to-anywhere flow rate of bio phosphorus is $\Phi_{\text{bio}}(\Omega \rightarrow \Omega) = 8.4 \text{ Tmol/year}$. Flow rates less than 0.1% of $\Phi_{\text{bio}}(\Omega \rightarrow \Omega)$ have been omitted for clarity.

The shortest mean sequestration times for exit in the Southern Ocean are associated with nutrient trapping, while the longest mean sequestration times are for paths from the North Pacific, where the biogenic particle transport injects phosphorus into very old waters. The mean sequestration time of bio phosphorus that first reemerges (as regenerated PO_4 or remineralizing DOP) in the Southern Ocean (SAAD and NAAD) euphotic zone, regardless of the location of last utilization, is 240 ± 60 years. Bio pipes from the Southern Ocean are associated with relatively long time scales if they start in the SAAD region associated with southward transport and Antarctic Bottom Water (AABW) formation, and with relatively short time scales if they start in the NAAD region associated with northward Ekman transport and mode and intermediate waters. The exception are the NAAD-to-North Pacific pipes, which have roughly 1200 year mean sequestration times because of the very weak upwelling in the North Pacific. Short return time scales of decades or less characterize all diagonal elements of Figure 7 because of the very high flow rates associated with eddy-diffusive return flow.

The global $\Omega \rightarrow \Omega$ sequestration time scale is 130 ± 70 years, set by global biological production and the inventory of bio phosphorus (equivalently, by the pump efficiency). The longest mean phosphorus ages on exit regardless of where entry occurred ($\Omega \rightarrow \Omega_f$) are 430 ± 30 years for exit in SAAD, 210 ± 80 years for exit in the subpolar North Pacific, and 150 ± 50 years for exit in NAAD. All other regions have anywhere-to- Ω_f mean sequestration times that are significantly shorter (10–100 years). This pattern arises because the Southern Ocean and subpolar North Pacific reexpose both very old waters and nutrients, while the EEqP upwells old waters but also a significant proportion of relatively recently exported nutrients, leading to relatively long sequestration times for the subpolar regions and relatively short sequestration times for equatorial upwelling regions. Remarkably, the phosphorus mean age on exit anywhere (i.e., $\Omega_i \rightarrow \Omega$) is in the 100–180 years range and insensitive to where entry occurred. This restates the fact that the $\Omega_i \rightarrow \Omega$ flow rates and bio phosphorus masses are approximately proportional, as noted above. A similar feature was also evident in the study by DeVries *et al.* [2012], where a map of grid box $\rightarrow \Omega$ sequestration times shows little variation across the globe around a value of roughly 150 years except at the localized deep-water formation regions in the North Atlantic and Weddell Sea, where the sequestration time is much longer (exceeding 400

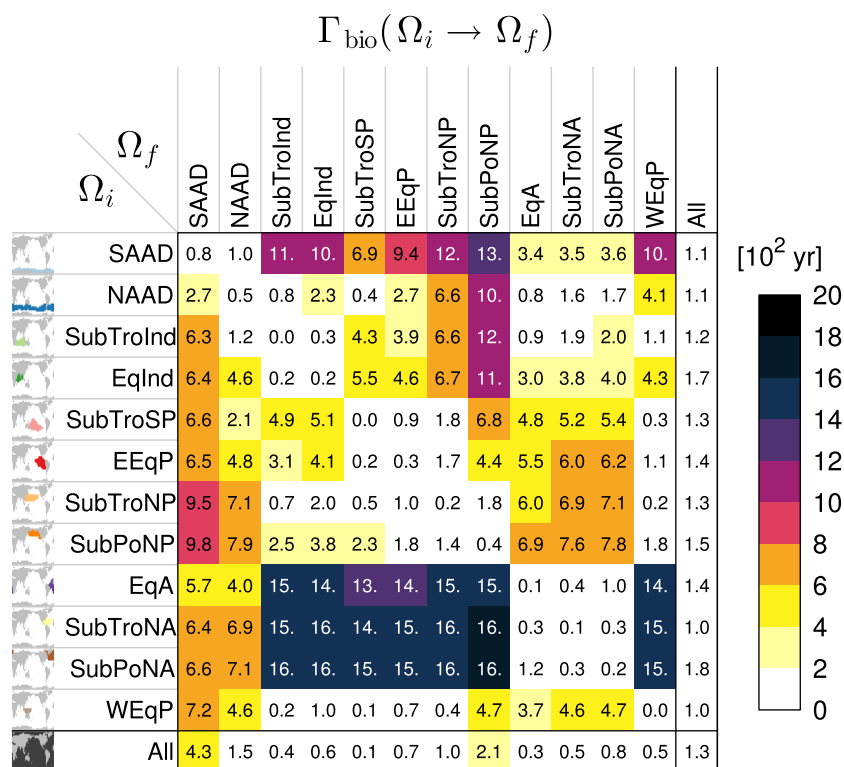


Figure 7. The mean sequestration times, Γ_{bio} , of the $\Omega_i \rightarrow \Omega_f$ bio pipes organized as in Figure 4. The mean sequestration times of the $\Omega \rightarrow \Omega_f$ and $\Omega_i \rightarrow \Omega$ bio pipes have been included as a separate row and column, respectively.

years in the study of DeVries *et al.* [2012]). These localized effects are averaged out for our flow rates that are calculated for the large regions of Figure 2.

Although the $\Omega_i \rightarrow \Omega_f$ masses, flow rates, and mean sequestration times give an indication of the nature of the nutrient paths taken by the bio phosphorus, the detailed spatial pathways through the ocean interior, determined by both biogenic and physical transport, are not obvious a priori. We therefore quantify the three-dimensional, transit-time partitioned paths of the bio pipes by computing their path density.

5.5. Path Densities

The path density $\eta_{\text{bio}}(\mathbf{r}|\tau : \Omega_i \rightarrow \Omega_f)d\tau$ is simply the concentration of bio phosphorus molecules at point \mathbf{r} that are in transit from last utilization in Ω_i to first reemergence into Ω_f (as regenerated PO_4 or remineralizing DOP) in transit-time interval $(\tau, \tau+d\tau)$. Because each bio phosphorus molecule traces out a path from Ω_i to Ω_f , this concentration is also the density of these paths [Holzer and Primeau, 2006, 2008, 2013]. In steady state, this path density is efficiently computed using forward and adjoint Green functions of the phosphorus tracer equations as detailed in Appendices A and B.

Because the path density is very information rich, we focus on the six most massive $\Omega_i \rightarrow \Omega_f$ bio pipes (i.e., on those with the largest $\mu_{\text{bio}}(\Omega_i \rightarrow \Omega_f)$). To summarize the transit-time dependence of the path density, we first analyze the transit-time partitioned mass of bio phosphorus in the pipes, which is given by $\mathcal{R}_{\text{bio}}(t : \Omega_i \rightarrow \Omega_f) = \int d^3\mathbf{r} \eta_{\text{bio}}(\mathbf{r}|t : \Omega_i \rightarrow \Omega_f)$, so that $\mu_{\text{bio}}(\Omega_i \rightarrow \Omega_f) = \int_0^\infty dt \mathcal{R}_{\text{bio}}(t : \Omega_i \rightarrow \Omega_f)$ (see Appendix A).

Figure 8 shows the transit-time partitioned mass \mathcal{R}_{bio} plotted with a logarithmic time axis to show the full distribution. The mode of these distributions, except for the self-connected NAAD \rightarrow NAAD case, lies roughly between 200 and 400 years. For the NAAD \rightarrow SAAD, NAAD \rightarrow NAAD, and EqA \rightarrow SAAD cases, a secondary mode can be seen around residence times between 1000 and 2000 years. Basin integrals of the path density (see Appendix D) reveal that this secondary mode is due to deep bimodal Pacific paths: A century time scale mode is associated with the deep overturning cell [Lumpkin and Speer, 2007], while a millennial mode is presumably associated with advective-diffusive paths that stagnate in the old waters of the deep

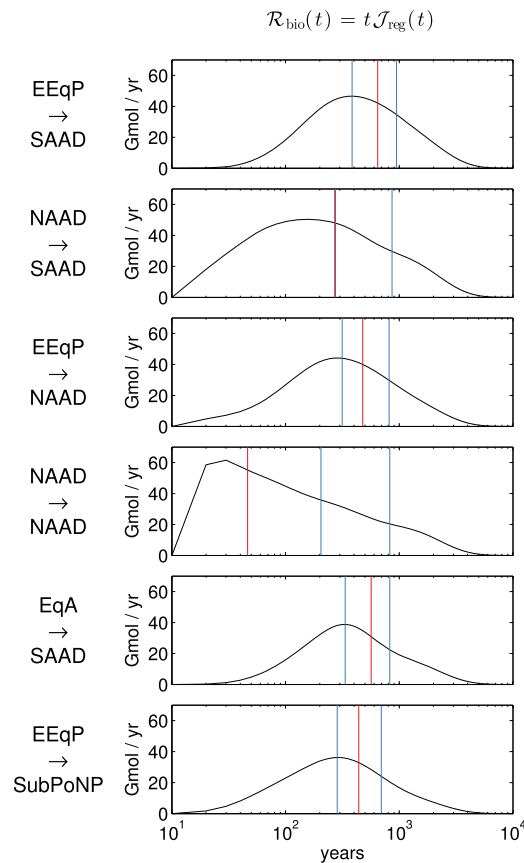


Figure 8. The residence-time distributions $\mathcal{R}_{\text{bio}}(t) = t \mathcal{J}_{\text{reg}}(t)$ for the bio pipes with the six dominant masses $\mu_{\text{bio}}(\Omega_i \rightarrow \Omega_f)$. The mean sequestration time (phosphorus mean age on exit), Γ_{bio} , is indicated as a red line and the first and third septiles of \mathcal{R}_{bio} are indicated as vertical blue lines.

the mode of \mathcal{R}_{bio} , while the third septile lies between 700 and 1000 years. The mean sequestration time, Γ_{bio} , falls between the first and third septiles, except for the overlapping NAAD \rightarrow NAAD and abutting NAAD \rightarrow SAAD cases. For the NAAD \rightarrow NAAD case, Γ_{bio} is much shorter than the first septile and close to the decadal mode.

Figure 9 displays the global zonal averages of the path density η_{bio} integrated over the fast, medium, and slow transit-time bands, respectively. Note that the local magnitude of the time-integrated path density is directly proportional to its contribution to the biological pump efficiency. Because of their order 1000-year time scale, the slow paths tend to lie in the abyssal ocean, are highly eddy-diffusive, and disperse the bio phosphorus they carry throughout the world oceans. The fast paths tend to be concentrated in the directly wind-driven thermocline. The EqA \rightarrow SAAD paths are the exception with fast paths that are more diffusive and access upwelling Circumpolar Deep Water (CDW). Because of the eddy-diffusive component of the transport, a general feature of the $\Omega_i \rightarrow \Omega_f$ path density for nonoverlapping origin and receptor regions is that it goes to zero close to both Ω_i and Ω_f . This is because phosphorus molecules close Ω_i tend to trace out $\Omega_i \rightarrow \Omega_i$ paths, and those close to Ω_f tend to trace out $\Omega_f \rightarrow \Omega_f$ paths [Holzer, 2009; Holzer and Primeau, 2006, 2008, 2013].

Figure 9 shows that the density class ($27.0 < \sigma_\theta < 27.6$) kg m^{-3} , broadly associated with AAIW [Talley, 1996], carries a significant fraction of the bio phosphorus exported from the Eastern Equatorial Pacific (EEqP) that is destined for the Southern Ocean, with a similar pattern for destinations SAAD and NAAD. Volume integrating η_{bio} , we find that the AAIW density class carries $\sim 50\%$ of the fast and medium EEqP \rightarrow SO paths. Regardless of transit time, the AAIW density class carries $\sim 35\%$ of all EEqP \rightarrow SO bio phosphorus, with the remaining $\sim 65\%$ being carried by denser water, including CDW that upwells in the Southern

North Pacific [Holzer and Primeau, 2006, 2008]. Interestingly, basin integrals also show that the mass of bio phosphorus in transit from the Equatorial Atlantic to SAAD has greater contributions from paths in the Pacific and Indian Oceans than from paths in the Atlantic. Bio phosphorus on its way to Antarctica gets swept by the Antarctic Circumpolar Current into the Indian and Pacific Oceans, where some of it can recirculate for several centuries before reemerging in the SAAD euphotic zone. The distribution \mathcal{R}_{bio} for the NAAD \rightarrow NAAD case exhibits a very fast mode of ~ 2 decades and a very long broad tail. The fast mode is due to nutrient trapping and recirculation in mode and intermediate waters. The long tail has contributions from paths in all basins, with a bimodal contribution from the Pacific (century and millennial modes as discussed above).

To summarize the spatial pattern of the path density, we distinguish fast, medium, and slow transit times by the 1/7 and 3/7 quantiles (first and third septiles) of \mathcal{R}_{bio} . By definition, fast paths thus carry 1/7 of the bio phosphorus mass, medium paths carry 2/7 of the mass, and slow paths carry 4/7 of the mass in the $\Omega_i \rightarrow \Omega_f$ bio pipe, with proportional contributions to E_{bio} . While this definition of fast, medium, and slow transit-time bands is somewhat arbitrary, experimentation with different time bands showed that the first and third septiles are well positioned to separate out different flow regimes as quantified below. The first and third septiles are indicated on Figure 8. Except for the self-connected NAAD \rightarrow NAAD case, the first septile roughly tracks

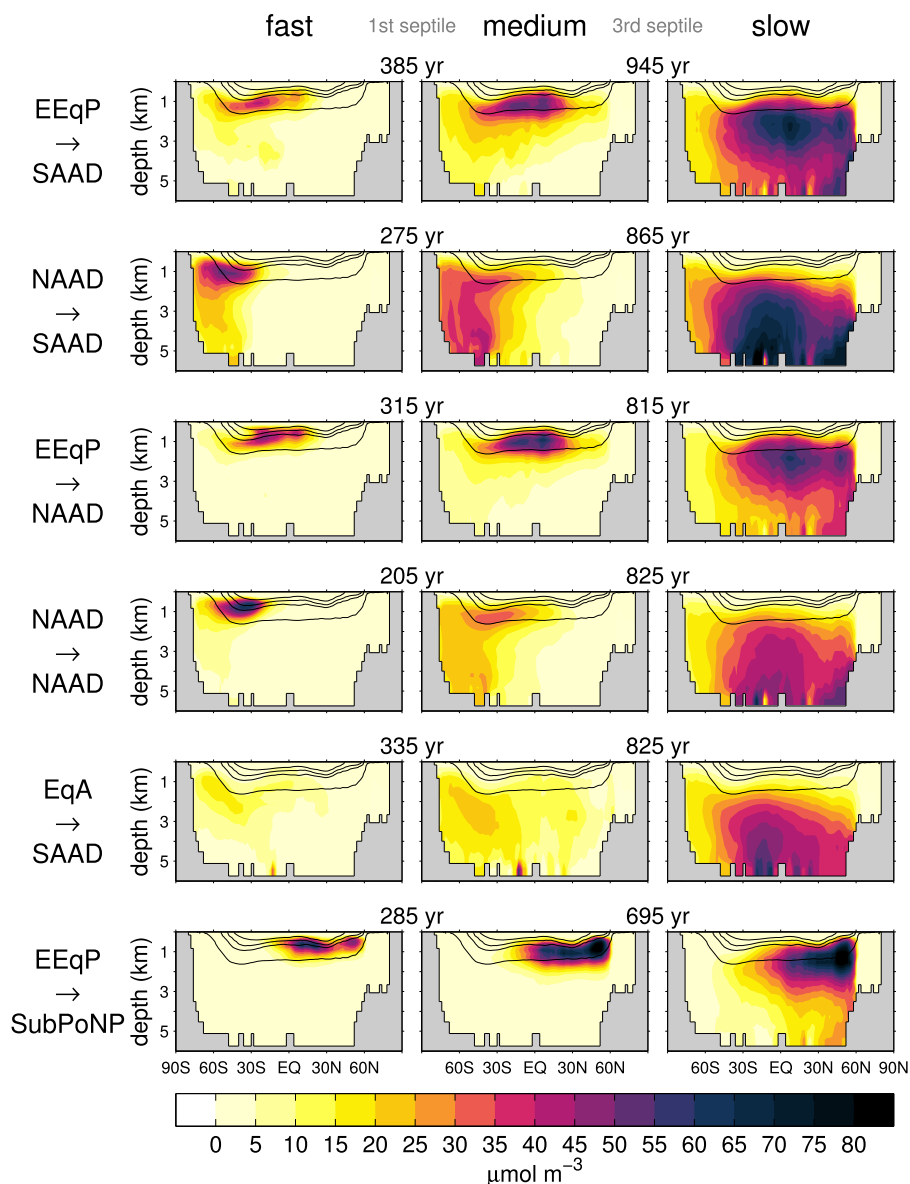


Figure 9. The path densities of the bio pipes with the six dominant masses $\mu_{\text{bio}}(\Omega_i \rightarrow \Omega_f)$, zonally averaged over the entire world ocean. These are the spatial patterns associated with the distributions of Figure 8. The path densities have been integrated over the fast, medium, and slow transit-time bands bounded by the first and third septiles of \mathcal{R}_{bio} indicated between the three panels of each $\Omega_i \rightarrow \Omega_f$ pathway. The black contours indicate the σ_0 isopycnals at 26.6, 27.0, 27.2, and 27.6 kg m^{-3} , with AAIW typically considered to lie between 27.0 and 27.6 kg m^{-3} .

Ocean. AAIW is commonly associated with the export of preformed nutrients out of the Southern Ocean [e.g., Sarmiento *et al.*, 2004; Palter *et al.*, 2010; Holzer *et al.*, 2014]. However, the bio phosphorus path density reveals that eddy diffusion and recirculation in these water masses additionally allows nutrients last exported into the deeper waters of the EEQp to return to the Southern Ocean euphotic zone. The path density furthermore shows that the long-time-scale EEQp \rightarrow SO pathways explore the entire world ocean, but are concentrated at mid depths in the North Pacific, which holds the ocean's oldest waters.

The paths connecting the Southern Ocean to itself that contribute most to E_{bio} (NAAD \rightarrow SAAD and NAAD \rightarrow NAAD) are confined to the Southern Ocean for the fast paths, with the NAAD \rightarrow SAAD paths extending deeper, presumably because return to the SAAD surface occurs through deep vertical mixing. At intermediate time scales, the NAAD \rightarrow SAAD paths access the deep SO and Antarctic Bottom Water with greater density than the NAAD \rightarrow NAAD paths, which are mostly concentrated in intermediate and mode waters. At

long time scales, both the NAAD \rightarrow SAAD and NAAD \rightarrow NAAD paths explore the abyssal ocean, with greater density for the NAAD \rightarrow SAAD paths as return to SAAD dictates access to the deep cell of the global overturning circulation.

Fast and medium time-scale paths from the Equatorial Atlantic to the SAAD region of the Southern Ocean (EqA \rightarrow SAAD) are dominated by upwelling CDW, while for long time scales these paths lie in the abyssal ocean. Finally, the paths from the Eastern Equatorial Pacific to the subpolar North Pacific (EEqP \rightarrow SubPoNP) are dominated by thermocline waters. For the EEqP \rightarrow SubPoNP paths, relatively little of the abyssal ocean is explored even for the slow transit-time band because most of the deep paths do not connect efficiently to the North Pacific surface [e.g., Schmitz, 1995; Toggweiler and Samuels, 1993; Sun and Bleck, 2001; Ganachaud and Wunsch, 2000].

6. Discussion and Conclusions

We have systematically analyzed the combined biogenic and physical transport of nutrients in the global ocean and how this transport determines the global efficiency of the biological pump, defined by the size of the global nonpreformed phosphorus pool. Nonpreformed phosphorus, which we have dubbed bio phosphorus, is comprised of regenerated phosphate and DOP. Unlike previous approaches that assess the importance of a particular region by perturbing its nutrient uptake (for example, by forcing complete utilization in the Southern Ocean) [e.g., Sarmiento *et al.*, 2004; Primeau *et al.*, 2013], and computing the resulting anomaly from the unperturbed base state, we have used synthetic Green-function tracers to assess the transport from and to specified regions within an unperturbed, data-assimilated estimate of the global phosphorus cycle. This has the advantage of diagnosing the nutrient cycle as it operates within the current climate, rather than diagnosing the response to altering the nutrient cycle, a response that is highly nonlinear in the perturbed biogeochemical parameters.

This work is closely related to that of DeVries *et al.* [2012] on sequestration efficiency. For the case where the destination region is not specified, and in the limit of instant remineralization (no DOP pool), Γ_{bio} is equal to the mean sequestration time introduced by DeVries *et al.* [2012]. In that case and limit, the flow rate Φ_{bio} reduces to the export production of Ω_i , and the transit-time partitioned flow rate \mathcal{J}_{bio} in the $\Omega_i \rightarrow \Omega$ bio pipe is proportional to the “sequestration efficiency” of DeVries *et al.* [2012]. Our approach here generalizes the results of DeVries *et al.* [2012] to the case of nonzero remineralization time scale (nonzero DOP pool), and to reexposure destinations Ω_f that are specified subregions of the global euphotic zone. The corresponding generalized sequestration efficiency of a given region is the cumulative form of the flow-rate distribution \mathcal{J}_{bio} developed here (see Appendix E where the precise connections are developed). Another key distinction with the work of DeVries *et al.* [2012] is that we diagnose the nutrient transport in terms of the interior “plumbing” of the biological pump, rather than solely in terms of the geographic surface distribution of the sequestration efficiency.

Our analysis provides a new view of the inner workings of the global biological pump that quantifies the importance of different geographic regions for pumping or leaking phosphorus, as well as the time scales and pathways interconnecting these regions. Our key findings are as follows:

1. While biological productivity alone is insufficient to guarantee high pump efficiency without correspondingly long sequestration times, the equatorial and subpolar regions of high productivity are nevertheless the largest contributors to the biological pump: the Eastern Equatorial Pacific (EEqP), North of the Antarctic Divergence (NAAD), Equatorial Atlantic (EqA), Subpolar North Pacific (SubPoNP), Subpolar North Atlantic (SubPoNA), and Equatorial Indian (EqInd) regions together account for $(77 \pm 7)\%$ of the pump efficiency.
2. Consistent with previous studies [DeVries *et al.*, 2012; Primeau *et al.*, 2013], the high-latitude regions are the largest leaks of the biological pump: the Southern Ocean (SAAD and NAAD), subpolar North Atlantic, and subpolar North Pacific, account for $(96 \pm 1)\%$ of the global pump leak. The SAAD and NAAD regions of the Southern Ocean make comparable contributions to the leak of $(43 \pm 4)\%$ and $(32 \pm 1)\%$, respectively.
3. Of the $14 \times 14 = 196$ possible $\Omega_i \rightarrow \Omega_f$ pathways of bio phosphorus (“bio pipes”) considered, a mere 11 carry $(52 \pm 6)\%$ of the biological pump efficiency (i.e., $(20 \pm 4)\%$ of the global bio phosphorus inventory). The bio pipes contributing most to E_{bio} connect the Eastern Equatorial Pacific and Equatorial Atlantic

oceans to the Southern Ocean ($21 \pm 3\%$), the Southern Ocean to itself ($15 \pm 3\%$), the Eastern Equatorial Pacific to the subpolar North Pacific ($4 \pm 1\%$), and the Eastern Equatorial Pacific to itself ($4 \pm 1\%$). By contrast, more than half ($53 \pm 2\%$) of the preformed inventory is carried by just the four preformed pipes that connect the Southern Ocean to itself.

4. The patterns with which remineralized bio phosphorus and preformed phosphate first reemerge into the euphotic zone are qualitatively similar. For both bio phosphorus and preformed phosphate, the dominant receptors are the SAAD and NAAD regions of the Southern Ocean, with significant secondary receptors in the equatorial and subpolar Pacific. ($69 \pm 1\%$) of the global preformed phosphate inventory and ($61 \pm 2\%$) of the global bio phosphorus inventory first reemerge as phosphate into the Southern Ocean euphotic zone. The similarity between bio and preformed reexposure patterns is likely due to the fact that particle transport injects bio phosphorus into the same deep waters that carry the bulk of preformed phosphate. Thus, preformed and bio phosphorus, while having different source distributions, reemerge with a similar geographic pattern.
5. The $\Omega_i \rightarrow \Omega_f$ flow rates of bio phosphorus are dominated by the $\Omega_i = \Omega_f$ "self-connections". This is a consequence of the top-loaded power-law distribution of DOP production and the eddy-diffusive nature of the physical circulation, which returns fluid elements to the surface after a short residence time in the interior [Primeau and Holzer, 2006; Hall et al., 2007]. The largest flow rates are associated with the NAAD \rightarrow NAAD and EEqP \rightarrow EEqP bio pipes, which contribute ($16 \pm 3\%$) and ($16 \pm 4\%$), respectively, to the global anywhere-to-anywhere flow of bio phosphorus, but only ($5 \pm 1\%$) and ($4 \pm 1\%$), respectively, to the efficiency of the biological pump.
6. The mean sequestration time (phosphorus mean age on exit) for the global anywhere-to-anywhere bio pipe is 130 ± 70 years, set by the global export production and the efficiency of the biological pump. Bio pipes connecting the North and Equatorial Atlantic to the Indian and Pacific Oceans follow the deep diffusive conveyor circulation [Holzer and Primeau, 2006, 2008] and have mean sequestration times of ~ 1300 – 1600 years. Including all possible export regions (i.e., anywhere-to- Ω_f bio pipes), the Southern Ocean and the subpolar North Pacific have the longest mean ages on exit (~ 150 – 430 years). All other regions have anywhere-to- Ω_f mean ages on exit that are significantly shorter (~ 10 – 100 years). The phosphorus mean age on exit anywhere (i.e., Ω_i -to-anywhere) is relatively insensitive to where entry occurred at values ranging 100–180 years, reflecting an approximate proportionality between the $\Omega_i \rightarrow \Omega_f$ flow rates and bio phosphorus masses. Perturbations in biological productivity are thus expected to affect the nutrient supply across the globe on a time scale of about a century.
7. The path density of bio phosphorus allowed us to quantify the three-dimensional structure of the bio pipes. Distinct patterns were identified for the fast, intermediate, and slow paths, defined so that they carry 1/7, 2/7, and 4/7 of the bio phosphorus mass in the pipes. For the most massive, non-self-connected bio pipes, the fast paths have transit times less than ~ 300 – 400 years, while the slow paths have transit times longer than ~ 700 – 900 years. The fast paths are generally concentrated in the thermocline, medium paths additionally access upwelling CDW, while the slow paths tend to explore most of the deep ocean. Southern Ocean self-connected slow paths and slow paths to the SAAD region of the Southern Ocean tend to be concentrated in the abyssal ocean, while other major slow paths tend to be concentrated in the very old waters of the middepth North Pacific.
8. The path density revealed that the dominant bio pipes from the Eastern Equatorial Pacific to the Southern Ocean (SAAD and NAAD) carry about a third of their bio phosphorus mass in the density class associated with AAIW, while the rest is carried by denser waters, including CDW. Particle export of bio phosphorus in the equatorial Pacific accesses these water masses in which the phosphorus can return to the Southern Ocean via eddy diffusion and gyre recirculation. Thus, the Southern Ocean not only supplies tropical and Northern Hemisphere waters with preformed nutrients via mode and intermediate waters but also receives a significant amount of regenerated nutrients via AAIW.

Our study has a number of limitations that should be kept in mind. Chief among these is that our circulation is steady. While the circulation represents a ventilation-weighted time average whose transport was optimized to reproduce annual-mean tracer observations, our analysis cannot capture covariances between seasonal biological productivity and seasonal physical flow. Our model also has coarse resolution and production in shallow shelf areas (less deep than the euphotic zone) has not been captured [Primeau et al., 2013]. The phosphorus cycle itself makes approximations such as a globally uniform Martin exponent and a single remineralization time scale [Kwon and Primeau, 2006; Primeau et al., 2013]. In a future study we plan

to relax some of these approximations and to explore how the plumbing of the biological pump responds to perturbations in the micronutrient supply by dynamically coupling the phosphorus and iron cycles.

Appendix A: Origin/Destination and Transit-Time Partitioned Phosphorus

Following *Holzer and Primeau* [2013], the contribution to P_{reg} from production in region Ω_i a time t ago during time interval dt , denoted as $dt g_{\text{reg}}(\mathbf{r}, t|\Omega_i)$ so g_{reg} is a distribution with respect to t , is given by

$$g_{\text{reg}}(\mathbf{r}, t|\Omega_i) = \int d^3\mathbf{r}' G_{\text{IO}}(\mathbf{r}, t|\mathbf{r}', 0) SJ(\mathbf{r}') \Omega_i(\mathbf{r}'), \quad (\text{A1})$$

where $d^3\mathbf{r}'$ is the volume element with respect to \mathbf{r}' and the integral is over the entire ocean. The mask Ω_i is unity everywhere beneath surface patch Ω_i . Similarly, the contribution to P_{O} from production in Ω_i a time t ago during dt , denoted as $dt g_{\text{O}}(\mathbf{r}, t|\Omega_i)$, is given by

$$g_{\text{O}}(\mathbf{r}, t|\Omega_i) = \int d^3\mathbf{r}' G_{\text{OO}}(\mathbf{r}, t|\mathbf{r}', 0) SJ(\mathbf{r}') \Omega_i(\mathbf{r}'). \quad (\text{A2})$$

The contribution to the bio phosphorus field is thus given by $g_{\text{bio}} \equiv g_{\text{reg}} + g_{\text{O}}$.

The preformed phosphate last in contact with the euphotic zone in Ω_i during dt a time t ago is given by $dt g_{\text{pre}}(\mathbf{r}, t|\Omega_i)$, where g_{pre} satisfies [*Holzer et al.*, 2012]

$$(\partial_t + \mathcal{T}) g_{\text{pre}}(\mathbf{r}, t|\Omega_i) = -\gamma_0(\mathbf{r}) [g_{\text{pre}}(\mathbf{r}, t|\Omega_i) - \delta(t) P_1(\mathbf{r}) \Omega_i(\mathbf{r})], \quad (\text{A3})$$

where $\gamma_0(\mathbf{r})$ is only nonzero for points \mathbf{r} in the euphotic zone, where $\gamma_0^{-1} = 1$ s, ensuring fast relaxation to the boundary conditions. The Dirac delta function acts as a source of preformed PO_4 , and for $t > 0$, the fast relaxation ensures that all preformed PO_4 reemerging into the euphotic zone is quickly set to zero. We thus obtain

$$g_{\text{pre}}(\mathbf{r}, t|\Omega_i) = \int d^3\mathbf{r}' G_{\text{II}}(\mathbf{r}, t|\mathbf{r}', 0) \gamma_0(\mathbf{r}') P_1(\mathbf{r}') \Omega_i(\mathbf{r}'). \quad (\text{A4})$$

Note that here γ_0 controls both the source and sink for G_{II} .

The inventories μ_X (total mass or moles of phosphorus) for $X = \text{pre, reg, or O}$ are given by

$$\mu_X(\Omega_i) = \int_0^\infty dt \int d^3\mathbf{r} g_X(\mathbf{r}, t|\Omega_i). \quad (\text{A5})$$

The total mass of bio phosphorus last taken up on Ω_i is $\mu_{\text{bio}}(\Omega_i) = \mu_{\text{reg}}(\Omega_i) + \mu_{\text{O}}(\Omega_i)$. The total phosphorus inventory is given by $\mu_{\text{P}} = \sum_i [\mu_{\text{bio}}(\Omega_i) + \mu_{\text{pre}}(\Omega_i)]$.

A1. Phosphorus Flow Rates and Time Scales

The flow rate of regenerated or preformed phosphate newly emerging into the euphotic zone of Ω_f , partitioned according to transit time and origin Ω_i follows from (A1) and (A4) as

$$dt \mathcal{J}_X(t : \Omega_i \rightarrow \Omega_f) \equiv dt \int d^3\mathbf{r} \Omega_f(\mathbf{r}) \gamma_0(\mathbf{r}) g_X(\mathbf{r}, t|\Omega_i), \quad (\text{A6})$$

where $X = \text{pre or reg}$. We note that all DOP remineralizing en route to, or within Ω_f is accounted for by g_{reg} and hence by \mathcal{J}_{reg} .

The masses of bio and preformed phosphorus transiting from $\Omega_i \rightarrow \Omega_f$ with a transit time in the interval $(t, t + dt)$ are thus given by

$$dt \mathcal{R}_{\text{bio}} = t dt \mathcal{J}_{\text{reg}} \quad \text{and} \quad dt \mathcal{R}_{\text{pre}} = t dt \mathcal{J}_{\text{pre}}. \quad (\text{A7})$$

The total $\Omega_i \rightarrow \Omega_f$ mass and flow rate of bio phosphorus regardless of transit time are obtained as

$$\mu_{\text{bio}}(\Omega_i \rightarrow \Omega_f) = \int dt \mathcal{R}_{\text{bio}}(t : \Omega_i \rightarrow \Omega_f), \quad (\text{A8})$$

$$\Phi_{\text{bio}}(\Omega_i \rightarrow \Omega_f) = \int dt \mathcal{J}_{\text{bio}}(t : \Omega_i \rightarrow \Omega_f). \quad (\text{A9})$$

The mean age on exit of bio phosphorus, equal to the mean sequestration time in steady state, is given by

$$\Gamma_{\text{bio}} = \frac{\langle t \mathcal{J}_{\text{bio}}(t) \rangle}{\langle \mathcal{J}_{\text{bio}}(t) \rangle} = \frac{\mu_{\text{bio}}}{\Phi_{\text{bio}}}, \quad (\text{A10})$$

where $\langle x(t) \rangle \equiv \int_0^\infty x(t) dt$.

A2. Phosphorus Path Density

The fraction of PO_4 at (\mathbf{r}, t) that will reemerge as phosphate in Ω_f after a transit time in the interval $(\tau, \tau + d\tau)$ is denoted by $d\tau \tilde{G}_1(\mathbf{r}, \tau - t | \Omega_f)$. The corresponding fraction of DOP is denoted by $d\tau \tilde{G}_0(\mathbf{r}, \tau - t | \Omega_f)$. These quantities are given by

$$\tilde{G}_1(\mathbf{r}, \tau - t | \Omega_f) = \int d^3 \mathbf{r}' \Omega_f(\mathbf{r}') \gamma_0(\mathbf{r}') G_{11}(\mathbf{r}', \tau - t | \mathbf{r}, 0), \quad (\text{A11})$$

and

$$\tilde{G}_0(\mathbf{r}, \tau - t | \Omega_f) = \int d^3 \mathbf{r}' \Omega_f(\mathbf{r}') \gamma_0(\mathbf{r}') G_{10}(\mathbf{r}', \tau - t | \mathbf{r}, 0), \quad (\text{A12})$$

where the fast relaxation with rate constant γ_0 captures PO_4 first reemerging in the euphotic zone of Ω_f .

The $\Omega_i \rightarrow \Omega_f$ path density is now simply given by the $\Omega_i \rightarrow \mathbf{r}$ phosphorus contribution g multiplied by the $\mathbf{r} \rightarrow \Omega_f$ arrival fraction \tilde{G} integrated over all possible intermediate times [Holzer and Primeau, 2006, 2013]:

$$\eta_{\text{reg}}(\mathbf{r} | \tau : \Omega_i \rightarrow \Omega_f) = \int_0^\tau dt \tilde{G}_1(\mathbf{r}, \tau - t | \Omega_f) g_{\text{reg}}(\mathbf{r}, t | \Omega_i), \quad (\text{A13})$$

and

$$\eta_0(\mathbf{r} | \tau : \Omega_i \rightarrow \Omega_f) = \int_0^\tau dt \tilde{G}_0(\mathbf{r}, \tau - t | \Omega_f) g_0(\mathbf{r}, t | \Omega_i), \quad (\text{A14})$$

where τ is the $\Omega_i \rightarrow \Omega_f$ transit, and hence residence, time. The path density of bio phosphorus is given by $\eta_{\text{bio}} = \eta_{\text{reg}} + \eta_0$.

We note that $\int d^3 \mathbf{r} \eta_{\text{bio}}(\mathbf{r} | t : \Omega_i \rightarrow \Omega_f) = \mathcal{R}_{\text{bio}}(t : \Omega_i \rightarrow \Omega_f)$, where the spatial integral is over the entire ocean domain. This follows from the definition of the path density in terms of the Green functions of the forward and time-reversed adjoint phosphate cycles, and the Chapman-Kolmogorov identity [e.g., Holzer and Primeau, 2008, 2013].

Appendix B: Computational Methods

We apply the framework of Holzer and Primeau [2013, see their Appendix B]. The spatially discretized fields are organized into column vectors whose rows map to grid locations \mathbf{r} . The fields g_{pre} , g_{reg} , and g_0 therefore become N -element column vectors (denoted in bold) so that we can write

$$\mathbf{A} = \begin{bmatrix} \mathbf{T} + \mathbf{L}_0 & -\kappa \mathbf{I} \\ 0 & \mathbf{T} + \kappa \mathbf{I} \end{bmatrix}, \quad \text{and} \quad \mathbf{g} = \begin{bmatrix} \mathbf{g}_{\text{pre}} & \mathbf{g}_{\text{reg}} \\ 0 & \mathbf{g}_0 \end{bmatrix}, \quad (\text{B1})$$

where \mathbf{T} is the $N \times N$ discrete version of \mathcal{T} , $\mathbf{L}_0 \equiv \mathbf{diag}(\gamma_0)$, and \mathbf{I} is the $N \times N$ identity matrix. The matrix of distributions \mathbf{g} satisfies the initial value problem:

$$(\partial_t + \mathbf{A})\mathbf{g}(t) = 0 \quad \text{with} \quad \mathbf{g}(0) = \begin{bmatrix} \mathbf{L}_0 \mathbf{P}_1 \Omega_i & 0 \\ 0 & \mathbf{SLP}_1 \Omega_i \end{bmatrix}, \quad (\text{B2})$$

where Ω_i is an N -element column vector for the mask $\Omega_i(\mathbf{r})$, $\mathbf{P}_1 \equiv \mathbf{diag}(P_1)$, \mathbf{S} is the discretized matrix version of the operator \mathcal{S} , and $\mathbf{L} \equiv \mathbf{diag}(\gamma)$. To compute the fields $g_x(t)$, we time step (B2) from the initial condition using a Crank-Nicholson scheme. Multiplying on the left by $\Omega_i^T \mathbf{V}$, where \mathbf{V} is the diagonal matrix of

volume elements $d^3\mathbf{r}$, corresponds to the volume integral on the mask $\Omega_f(\mathbf{r})$, therefore the field $\mathcal{J}_X(t)$ can be directly computed from $\mathbf{g}(t)$ by multiplying its components on the left by $\Omega_f^T \mathbf{V} \mathbf{L}_0$ for the inorganic part. $\mathcal{R}_{\text{bio}}(t)$ follows from (A7). Integrating (B2) over all times yields

$$\mathbf{A}\langle\mathbf{g}(t)\rangle=\mathbf{g}(0), \tag{B3}$$

which can be solved for $\langle\mathbf{g}(t)\rangle$ by direct matrix inversion. The flow rates Φ_X are computed by multiplying (B3) from the left by $\Omega_f^T \mathbf{L}_0$. Computing μ_X requires the moment $\langle t\mathbf{g}(t)\rangle$, which is the solution to

$$\mathbf{A}\langle t\mathbf{g}(t)\rangle=\langle\mathbf{g}(t)\rangle, \tag{B4}$$

obtained by multiplying (B2) by t and integrating over t . Equation (B4) can be solved for $\langle t\mathbf{g}(t)\rangle$ by direct inversion.

We calculate the distributions $\tilde{\mathcal{G}}_I$ and $\tilde{\mathcal{G}}_O$ similarly, but use an adjoint approach for computational efficiency so that we need only one tracer per patch Ω_f rather than one tracer per interior point \mathbf{r} . Organizing the spatial field $\tilde{\mathcal{G}}_X$ into column vector $\tilde{\mathcal{G}}_X$, we define

$$\tilde{\mathcal{G}}=\begin{bmatrix} \tilde{\mathcal{G}}_I \\ \tilde{\mathcal{G}}_O \end{bmatrix} \quad \text{and} \quad \tilde{\mathbf{A}}=\begin{bmatrix} \tilde{\mathbf{T}}+\mathbf{L}_0 & 0 \\ -\kappa\mathbf{I} & \tilde{\mathbf{T}}+\kappa\mathbf{I} \end{bmatrix}, \tag{B5}$$

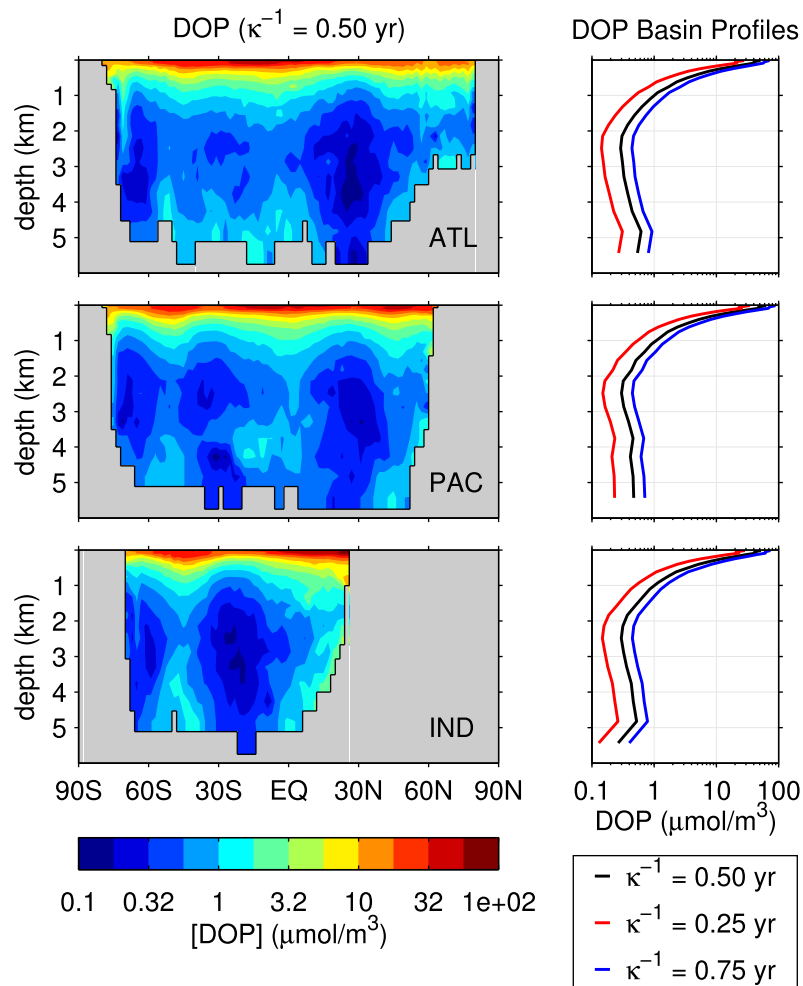


Figure C1. (left) Zonally averaged DOP concentrations for each ocean basin (ATL, PAC, and IND). Note the logarithmic color scale. (right) Corresponding basin-mean DOP profiles for the base state with $\kappa^{-1}=0.5$ year, and for $\kappa^{-1}=0.25$ and 0.75 year.

where $\tilde{\mathbf{T}} \equiv \mathbf{V}^{-1} \mathbf{T}^T \mathbf{V}$ is the adjoint of \mathbf{T} with respect to the volume-weighted inner product, and \mathbf{V} is the diagonal matrix of grid volumes $d^3 \mathbf{r}$. $\tilde{\mathcal{G}}$ satisfies the adjoint final-value problem:

$$(-\partial_t + \tilde{\mathbf{A}}) \tilde{\mathcal{G}}(t) = 0 \quad \text{with} \quad \tilde{\mathcal{G}}(0) = \begin{bmatrix} \mathbf{V} \mathbf{L}_0 \Omega_f \\ 0 \end{bmatrix}, \quad (\text{B6})$$

which we time-step backward from the final value $\tilde{\mathcal{G}}(0)$. Note that this evolves $\tilde{\mathcal{G}}(t)$ in the time-reversed adjoint flow from the final value. Without this adjoint technique, one would need to go through the expensive computation of the full $2N \times 2N$ matrix of $\mathbf{G}(\mathbf{r}, t | \mathbf{r}', 0)$ to obtain $\tilde{\mathcal{G}}(t)$. Integrating (26) over time, we get

$$\tilde{\mathbf{A}} \langle \tilde{\mathcal{G}}(t) \rangle = \tilde{\mathcal{G}}(0), \quad (\text{B7})$$

which we solve for $\langle \tilde{\mathcal{G}}(t) \rangle$ by direct inversion.

The discrete versions of the path densities $\eta_X(t)$ are computed by the convolution of the element-wise product of the time-stepped $\mathbf{g}(t)$ and $\tilde{\mathcal{G}}(\tau - t)$. The time-integrated path densities $\langle \eta_X(t) \rangle$ are computed as the element-wise product of $\langle \mathbf{g}(t) \rangle$ and $\langle \tilde{\mathcal{G}}(t) \rangle$ using a change in the order of integration.

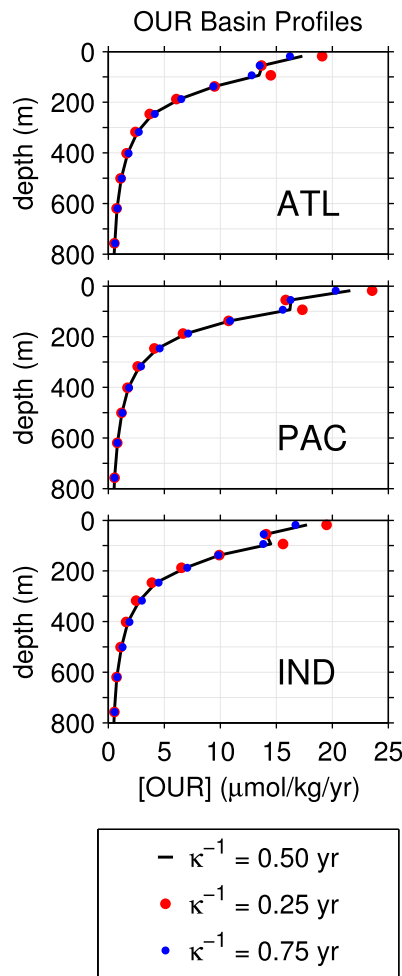


Figure C2. Basin-mean profiles of the model's phosphate remineralization rate per unit volume, $\kappa[\text{DOP}]$, expressed as oxygen utilization rate $[\text{OUR}] = R_{\text{O}_2:\text{P}} \kappa[\text{DOP}]$, with $R_{\text{O}_2:\text{P}} = 170$. Shown is the base state for $\kappa^{-1} = 0.5$ year, together with solutions for $\kappa^{-1} = 0.25$ and 0.75 year.

Appendix C: Sensitivity of DOP and Phosphate Remineralization Rate

Here we quantify the sensitivity of the DOP concentration and of the phosphate remineralization field to the poorly known rate constant κ (inverse remineralization time scale). Figure C1 shows the DOP concentration zonally averaged over each basin for the base state with $\kappa^{-1} = 0.5$ year. The pattern of DOP is identical to that of oxygen utilization rate (OUR) plotted by *Primeau et al.* [2013] for the same model, using a constant stoichiometry of $R_{\text{O}_2:\text{P}} = 170$. The DOP concentration falls off rapidly with depth in accord with the divergence of the Martin particle-flux profile defining the operator S in equation (1). To quantify the sensitivity of DOP to the value of κ , Figure C1 also shows basin-mean profiles of DOP for $\kappa^{-1} = 0.25$ and 0.75 year (i.e., $\kappa = 4.0$ and 1.3 year^{-1}). These perturbed DOP profiles are to a good approximation given by $\pm 50\%$ of the base-state profile throughout the water column, which shows that the DOP concentration is approximately proportional to κ^{-1} .

While DOP itself is sensitive to κ , the steady-state phosphate distribution only depends on the phosphate remineralization rate per unit volume, κP_{O} . Figure C2 plots κP_{O} expressed as OUR using $[\text{OUR}] = R_{\text{O}_2:\text{P}} \kappa P_{\text{O}}$, with $R_{\text{O}_2:\text{P}} = 170$, for the base state and for the two perturbed cases with $\kappa = 4.0$ and 1.3 year^{-1} . The OUR in Figure C2 can be compared with the observational estimates of OUR by *Sonnerup et al.* [2013, 2015] for the Pacific. These observations show magnitudes of $\sim 10 \pm 5 \mu\text{mol kg}^{-1} \text{ yr}^{-1}$ around 100–200 m depth and a rapid decay to near zero by 800 m depth, consistent with our modeled OUR. Figure C2 also shows that the sensitivity of κP_{O} is roughly $\pm 5\%$ near the surface, consistent with the $\sim 10\%$ sensitivity of the self-connected flow rates to the same changes in κ .

Appendix D: Basin Integrals of the Bio Phosphorus Path Density

Figure D1 shows the path densities $\eta_{\text{bio}}(\mathbf{r} | t : \Omega_i \rightarrow \Omega_f)$ volume integrated over each ocean basin above and below 1000 m depth.

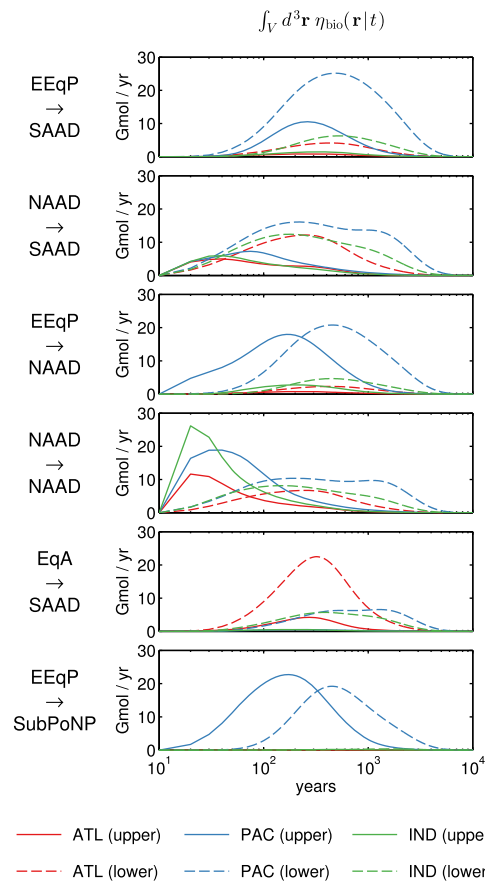


Figure D1. Volume integrals $\int_V d^3\mathbf{r} \eta_{\text{bio}}(\mathbf{r}|t)$ of the bio-phosphorus path density over the upper and deep Atlantic (red), Pacific (blue), and Indian Ocean (green). The solid lines indicate the integrals over the upper 1000 m of the basin, while the dashed lines indicate the integral over the basin below 1000 m depth.

For a given origin Ω_i and destination Ω_f , summing these integrals over all basins and over the upper and lower components gives the corresponding residence-time distribution $\mathcal{R}_{\text{bio}}(t : \Omega_i \rightarrow \Omega_f)$ shown in Figure 8. Further integrating the curves of Figure D1 over transit time quantifies the mass of bio phosphorus in $\Omega_i \rightarrow \Omega_f$ transit that resides in the upper or lower basin. (Note that Figure D1 has a logarithmic time axis so that the transit-time integral is not simply the area under the curve on the plot.)

Figure D1 shows that the phosphorus in the $\Omega_i \rightarrow \Omega_f$ bio pipes considered resides mostly below 1000 m depth, with residence times mostly of several centuries. As discussed in section 5.5, the deep Pacific distributions (dashed blue lines) of the NAAD \rightarrow SAAD, NAAD \rightarrow NAAD, and EqA \rightarrow SAAD bio pipes are bimodal, with a distinct millennial mode. The deep, slow bio-phosphorus paths are particularly important for E_{bio} because they carry a large portion of the global regenerated phosphate inventory. For the NAAD \rightarrow NAAD bio pipe, the partition between upper and lower paths confirms that the early decadal peak of its \mathcal{R}_{bio} distribution is due to nutrient trapping and recirculation in the upper Southern Ocean.

Appendix E: Connection With Sequestration Efficiency Distribution

The sequestration efficiency $\mathcal{E}(t|\Omega_i, t_i)$ of surface region Ω_i at time t_i defined by DeVries *et al.* [2012] is the fraction of the phosphate exported in Ω_i (generalized to bio phosphorus here) that has remained sequestered in the aphotic interior for a time t or longer, regardless of where it next reemerges into the euphotic zone. Note that Ω_i

can be shrunk to a single grid box or taken to the continuum limit when sums over patches become surface integrals. Here we develop the relation between $\mathcal{E}(t|\Omega_i, t_i)$ and our partitioned flow rates.

The bio phosphorus mass that was injected in Ω_i during time interval $(t_i, t_i + dt_i)$, and that remains in the ocean without emerging as phosphate into the euphotic zone for a time t or longer, can be obtained as the $\Omega_i \rightarrow \Omega$ flow rate \mathcal{J}_{bio} accumulated from time $t_i + t$ onward. Denoting this mass by $\phi_{\text{bio}} dt_i$ so that ϕ_{bio} has units of moles per unit injection time, we thus have

$$dt_i \phi_{\text{bio}}(t_i + t|\Omega_i, t_i) = dt_i \int_t^\infty dt' \mathcal{J}_{\text{bio}}(t_i + t'|\Omega_i \rightarrow \Omega, t_i). \tag{E1}$$

The total bio phosphorus (regardless of sequestration time) exported at Ω_i during $(t_i, t_i + dt_i)$ is given by $\Phi_{\text{bio}}(\Omega_i \rightarrow \Omega, t_i) dt_i$. Thus, by definition, and after cancelling the dt_i , we have

$$\mathcal{E}(t|\Omega_i, t_i) = \frac{\phi_{\text{bio}}(t_i + t|\Omega_i, t_i)}{\Phi_{\text{bio}}(\Omega_i \rightarrow \Omega, t_i)}. \tag{E2}$$

Using the relation (E1) between ϕ_{bio} and \mathcal{J}_{bio} , plus the fact that $\Phi_{\text{bio}}(\Omega_i \rightarrow \Omega, t_i) = \int_0^\infty dt' \mathcal{J}_{\text{bio}}(t_i + t'|\Omega_i \rightarrow \Omega, t_i)$, it is apparent that \mathcal{E} is the (complementary) cumulative distribution of the normalized transit-time partitioned flow rate \mathcal{J}_{bio} . It follows that $\Gamma_{\text{bio}}(\Omega_i \rightarrow \Omega, t_i) = \int_0^\infty \mathcal{E}(t|\Omega_i, t_i) dt$ and

$$\frac{\mathcal{J}_{\text{bio}}(t_i + t | \Omega_i \rightarrow \Omega, t_i)}{\Phi(\Omega_i \rightarrow \Omega, t_i)} = -\frac{\partial}{\partial t} \mathcal{E}(t | \Omega_i, t_i), \quad (\text{E3})$$

as can be verified analytically by explicit calculation.

In the model of *DeVries et al.* [2012], which carries no DOP and has a single-grid-layer euphotic zone (or represents the euphotic layer as a 2D surface in the continuum limit), the sequestration efficiency becomes independent of phosphate uptake and hence export production. This is because (i) without DOP, ϕ_{bio} becomes export production, and (ii) because with a single grid layer euphotic zone (or 2D euphotic surface), ϕ_{bio} becomes simply proportional to Φ_{bio} , which cancels in (E2).

Acknowledgments

We thank François Primeau for making the data-assimilated circulation and phosphorus cycle available to us. The data used to constrain the phosphorus cycling model are available from the World Ocean Atlas 09 (<https://www.nodc.noaa.gov/OC5/WOA09/wao09-data.html>). We thank Andreas Oschlies and Jonathan Lauderdale for reviews that led to an improved manuscript. This work was supported by grant DP120100674 from the Australian Research Council (M.H.). B.P. gratefully acknowledges scholarship support from the Government of Monaco, the Scientific Centre of Monaco, the Frères Louis et Max Principale Foundation, and the Cuomo Foundation.

References

- Archer, D. E., G. Eshel, A. Winguth, W. Broecker, R. Pierrehumbert, M. Tobis, and R. Jacob (2000), Atmospheric pCO₂ sensitivity to the biological pump in the ocean, *Global Biogeochem. Cycles*, *14*(4), 1219–1230, doi:10.1029/1999GB001216.
- Broecker, W. S. (1982), Ocean chemistry during glacial time, *Geochim. Cosmochim. Acta*, *46*, 1689–1705.
- DeVries, T. (2014), The oceanic anthropogenic CO₂ sink: Storage, air-sea fluxes, and transports over the industrial era, *Global Biogeochem. Cycles*, *28*, 631–647, doi:10.1002/2013GB004739.
- DeVries, T., and F. Primeau (2011), Dynamically and observationally constrained estimates of water-mass distributions and ages in the global ocean, *J. Phys. Oceanogr.*, *41*, 2381–2401, doi:10.1175/JPO-D-10-05011.1.
- DeVries, T., F. Primeau, and C. Deutsch (2012), The sequestration efficiency of the biological pump, *Geophys. Res. Lett.*, *39*, L13601, doi:10.1029/2012GL051963.
- Dutkiewicz, S., M. J. Follows, P. Heimbach, and J. Marshall (2006), Controls on ocean productivity and air-sea carbon flux: An adjoint model sensitivity study, *Geophys. Res. Lett.*, *33*, L02603, doi:10.1029/2005GL024987.
- Ganachaud, A., and C. Wunsch (2000), Improved estimates of global ocean circulation, heat transport and mixing from hydrographic data, *Nature*, *408*, 453–457.
- Hall, T. M., and M. Holzer (2003), Advective-diffusive mass flux and implications for stratosphere-troposphere exchange, *Geophys. Res. Lett.*, *30*(5), 1222, doi:10.1029/2002GL016419.
- Hall, T. M., T. W. N. Haine, M. Holzer, D. A. LeBel, F. Terenzi, and D. W. Waugh (2007), Ventilation rates estimated from tracers in the presence of mixing, *J. Phys. Oceanogr.*, *37*, 2599–2611, doi:10.1175/2006JPO3471.1.
- Holzer, M. (2009), The path density of interhemispheric surface-to-surface transport. Part I: Development of the diagnostic and illustration with an analytic model, *J. Atmos. Sci.*, *66*, 2159–2171, doi:10.1175/2009JAS2894.1.
- Holzer, M., and F. W. Primeau (2006), The diffusive ocean conveyor, *Geophys. Res. Lett.*, *33*, L14618, doi:10.1029/2006GL026232.
- Holzer, M., and F. W. Primeau (2008), The path-density distribution of oceanic surface-to-surface transport, *J. Geophys. Res.*, *113*, C01018, doi:10.1029/2006JC003976.
- Holzer, M., and F. W. Primeau (2013), Global teleconnections in the oceanic phosphorus cycle: Patterns, paths, and timescales, *J. Geophys. Res. Oceans*, *118*, 1775–1796, doi:10.1002/jgrc.20072.
- Holzer, M., C. Orbe, and F. W. Primeau (2012), Stratospheric mean residence time and mean age at the tropopause: Connections and implications for observational constraints, *J. Geophys. Res.*, *117*, D12314, doi:10.1029/2012JD017547.
- Holzer, M., F. W. Primeau, T. DeVries, and R. Matear (2014), The Southern Ocean silicon trap: Data-constrained estimates of regenerated silicic acid, trapping efficiencies, and global transport paths, *J. Geophys. Res.*, *119*, 313–331, doi:10.1002/2014JC009356.
- Howarth, R. W. (1988), Nutrient limitation of net primary production in marine ecosystems, *Annu. Rev. Ecol. Syst.*, *19*(1), 89–110, doi:10.1146/annurev.es.19.110188.000513.
- Ito, T., and M. J. Follows (2005), Preformed phosphate, soft tissue pump and atmospheric CO₂, *J. Mar. Res.*, *63*, 813–839.
- Kwon, E. Y., and F. Primeau (2006), Sensitivity and optimization study of a biogeochemistry ocean model using an implicit solver and in situ phosphate data, *Global Biogeochem. Cycles*, *20*, GB4009, doi:10.1029/2005GB002631.
- Lumpkin, R., and K. Speer (2007), Global ocean meridional overturning, *J. Phys. Oceanogr.*, *37*, 2550–2562, doi:10.1175/JPO3130.1.
- Marinov, I., A. Gnanadesikan, J. R. Toggweiler, and J. L. Sarmiento (2006), The Southern Ocean biogeochemical divide, *Nature*, *441*, 964–967, doi:10.1038/nature04883.
- Marinov, I., M. Follows, A. Gnanadesikan, J. L. Sarmiento, and R. D. Slater (2008a), How does ocean biology affect atmospheric pCO₂? Theory and models, *J. Geophys. Res.*, *113*, C07032, doi:10.1029/2007JC004598.
- Marinov, I., A. Gnanadesikan, J. L. Sarmiento, J. R. Toggweiler, M. Follows, and B. K. Mignone (2008b), Impact of oceanic circulation on biological carbon storage in the ocean and atmospheric pCO₂, *Global Biogeochem. Cycles*, *22*, GB3007, doi:10.1029/2007GB002958.
- Palter, J. B., J. L. Sarmiento, A. Gnanadesikan, J. Simeon, and R. D. Slater (2010), Fueling export production: Nutrient return pathways from the deep ocean and their dependence on the Meridional Overturning Circulation, *Biogeosciences*, *7*, 3549–3568, doi:10.5194/bg-7-3549-2010.
- Pelegri, J. L., and G. T. Csanady (1991), Nutrient transport and mixing in the Gulf Stream, *J. Geophys. Res.*, *96*(C2), 2577–2583.
- Pelegri, J. L., G. T. Csanady, and A. Martins (1996), The North Atlantic nutrient stream, *J. Oceanogr.*, *52*, 275–299.
- Primeau, F. W., and M. Holzer (2006), The ocean's memory of the atmosphere: Residence-time and ventilation-rate distributions of water masses, *J. Phys. Oceanogr.*, *36*, 1439–1456, doi:10.1175/JPO2919.1.
- Primeau, F. W., M. Holzer, and T. DeVries (2013), Southern Ocean nutrient trapping and the efficiency of the biological pump, *J. Geophys. Res. Oceans*, *118*, 2547–2564, doi:10.1002/jgrc.20181.
- Raven, J. A., and P. G. Falkowski (1999), Oceanic sinks for atmospheric CO₂, *Plant Cell Environ.*, *22*(6), 741–755, doi:10.1046/j.1365-3040.1999.00419.x.
- Sarmiento, J. L., N. Gruber, M. A. Brzezinski, and J. P. Dunne (2004), High-latitude controls of thermocline nutrients and low latitude biological productivity, *Nature*, *427*, 56–60.
- Schmitz, W. J. (1995), On the interbasin-scale thermohaline circulation, *Rev. Geophys.*, *33*(2), 151–173.
- Sigman, D. M., M. P. Hain, and G. H. Haug (2010), The polar ocean and glacial cycles in atmospheric CO₂ concentration, *Nature*, *466*(7302), 47–55.
- Smith, S. V. (1984), Phosphorus versus nitrogen limitation in the marine environment, *Limnol. Oceanogr.*, *29*(6), 1149–1160.

- Sonnerup, R. E., S. Mecking, and J. L. Bullister (2013), Transit time distributions and oxygen utilization rates in the northeast Pacific Ocean from chlorofluorocarbons and sulfur hexafluoride, *Deep Sea Res., Part I*, *72*, 61–71, doi:10.1016/j.dsr.2012.10.013.
- Sonnerup, R. E., S. Mecking, J. L. Bullister, and M. J. Warner (2015), Transit time distributions and oxygen utilization rates from chlorofluorocarbons and sulfur hexafluoride in the southeast Pacific Ocean, *J. Geophys. Res. Oceans*, *120*, 3761–3776, doi:10.1002/2015JC010781.
- Sun, S., and R. Bleck (2001), Thermohaline circulation studies with an isopycnic coordinate ocean model, *J. Phys. Oceanogr.*, *31*, 2761–2782.
- Talley, L. (1996), Antarctic intermediate water in the South Atlantic, in *The South Atlantic: Present and Past Circulation*, edited by G. Wefer et al., pp. 219–238, Springer, Berlin.
- Toggweiler, J. R., and B. Samuels (1993), New radiocarbon constraints on the upwelling of abyssal water to the ocean's surface, in *The Global Carbon Cycle, NATO ASI Ser. I, Global Environ. Change*, edited by M. Heinmann, pp. 333–366, Springer, N. Y.
- Trenberth, K. E., W. G. Large, and J. G. Olson (1989), A global ocean wind stress climatology based on ECMWF analyses, *Tech. Rep. TN-3381STR*, Natl. Cent. for Atmos. Res., Boulder Colo.
- Volk, T., and M. I. Hoffert (1985), Ocean carbon pumps: Analysis of relative strengths and efficiencies in ocean-driven atmospheric CO₂ changes, in *The Carbon Cycle and Atmospheric CO₂: Natural Variations Archean to Present, Geophys. Monogr. Ser.*, vol. 32, edited by E. T. Sundquist and W. S. Broecker, AGU, Washington, D. C.
- Williams, R. G., V. Roussenov, and M. J. Follows (2006), Nutrient streams and their induction into the mixed layer, *Global Biogeochem. Cycles*, *20*, GB1016, doi:10.1029/2005GB002586.
- Williams, R. G., E. McDonagh, V. M. Roussenov, S. Torres-Valdés, B. King, R. Sanders, and D. A. Hansell (2011), Nutrient streams in the North Atlantic: Advective pathways of inorganic and dissolved organic nutrients, *Global Biogeochem. Cycles*, *25*, GB4008, doi:10.1029/2010GB003853.